

A Plasma Torus Around a Young Low-Mass Star

Luke G. Bouma^{1,2}

¹*Observatories of the Carnegie Institution for Science, Pasadena, CA 91101, USA*

²*Department of Astronomy, California Institute of Technology, Pasadena, CA 91125, USA*

³*Carnegie Fellow; 51 Pegasi b Fellow*

A small fraction of red dwarfs younger than 100 million years show structured, periodic optical light curves suggestive of transiting opaque material that corotates with the star^{1–4}. However, the composition, origin, and even the existence of this material are uncertain. The main alternative hypothesis is that these complex periodic variables (CPVs) are explained by complex distributions of bright or dark regions on the stellar surfaces⁵. Here, we present time-series spectroscopy and photometry of a rapidly-rotating ($P=3.9$ hr) CPV, TIC 141146667. The spectra show sinusoidal time-varying Balmer emission at twice to four times the star’s equatorial velocity, which provides the first direct evidence for corotating plasma clumps around a CPV. While cool (10^4 K) plasma can persist within the hot (10^6 K) coronae of rapidly-rotating stars across a broad range of masses^{6–11}, our observations suggest that red dwarfs in particular can sustain long-lived, optically thick clumps that generate the sharp photometric features seen in CPVs. The origin of this optically thick material and its microphysical opacity remain unclear.

1 Main

M dwarfs, stars with masses below about half that of the Sun, are the only type of star to offer near-term prospects for detecting the atmospheres of rocky exoplanets with surface water¹². Community investment with JWST has proceeded accordingly^{13,14}. How an M dwarf’s evolution influences its planets—especially the retention of their atmospheres—has in turn become a major theme in exoplanet and stellar astrophysics. Previous work has established that most M dwarfs host close-in planets¹⁵ that on average are subject to long circumstellar disk lifetimes¹⁶, to high doses of UV radiation¹⁷, and to a high incidence of flares and coronal mass ejections¹⁸. However, despite extensive work in these areas, the plasma and magnetospheric environments that bathe young, close-in exoplanets remain challenging to quantify. Understanding these environments is crucial because they directly impact atmospheric retention and habitability of close-in planets.

One glaring example of our current ignorance is the complex periodic variables (CPVs). While Figure 1 highlights the main object of interest in this article, over one hundred analogous objects have now been found by K2 and TESS^{1–4,19,20}. These CPVs are phenomenologically identified based on their structured, periodic optical light curves; most are M dwarfs with rotation periods shorter than two days. Within current sensitivity limits, none host disks^{2,4}. However, $\approx 3\%$ of stars a few million years old show this complex photometric behavior, an observed fraction which decreases to $\approx 0.3\%$ by ≈ 150 Myr²⁰. CPVs are a known source of astrophysical false positives in searches for transiting exoplanets around young M dwarfs^{21–23}.

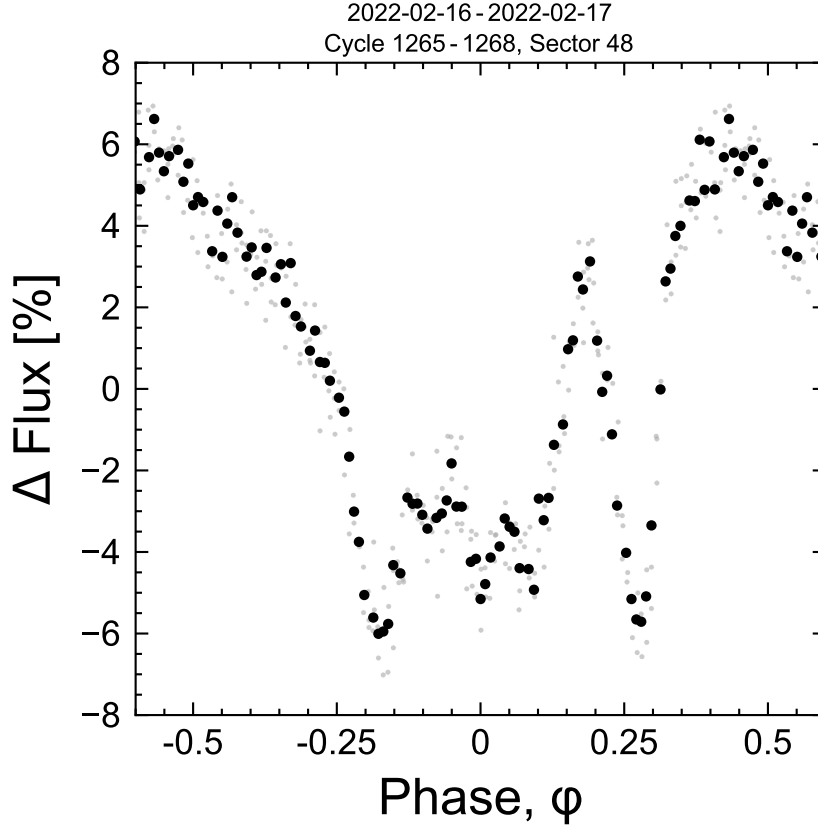


Figure 1 (Movie): TIC 141146667 is a complex periodic variable (CPV). The online movie, available [here](#), covers a baseline of 5,784 cycles irregularly sampled over three years. The TESS light curve is phased to the 3.930 hour period in groups of three cycles per frame. This is the period both of stellar rotation, and (we hypothesize) of corotating clumps of circumstellar material. Raw data acquired with two minute sampling are in gray; black averages to 100 points per cycle. Similar to other stars of this class, the sharp photometric features persist for tens to thousands of rotational cycles.

The two leading hypotheses for explaining CPVs are either that transiting clumps of circumstellar material corotate with the star^{2,4,24}, or that these stars represent an extreme in naturally-occurring distributions of starspots or faculae⁵. The main argument against a starspot-only explanation invokes the timescales and amplitudes of the sharpest photometric features. However, no independent evidence has yet been acquired for the presence of any circumstellar material. Geometrically, transiting clumps would imply an occurrence a few to at most ten times the observed rate. The clumps could therefore exist around 10-30% of M dwarfs during their early lives.

The dearth of evidence for circumstellar material around CPVs is surprising given that separate studies of young stars have, for decades, reported that stellar coronae contain both hot (10^6

K) and cool (10^4 K) plasma. In particular, time-series spectroscopy of stars with a wide range of masses has shown periodic high-velocity absorption and emission in Balmer lines such as $H\alpha$, interpreted as long-lived, corotating clumps of cool plasma^{6,8,25–30}. Such clumps are thought to be forced into corotation by the magnetic field, and the exact geometry of where the plasma can accumulate is dictated by the field’s topology. For instance, a magnetic dipole field tilted with respect to the stellar spin axis yields accumulations in a warped torus geometry⁷, whereas in the limit of a single strong field line, accumulation occurs at the line’s apex, furthest from the star¹⁰. To date, none of these spectroscopic variables have shown any photometric anomalies⁴, leaving open the issue of whether they are related to CPVs.

In this study, we present the first spectroscopic detection of corotating clumps of cool plasma around a CPV. We identified TIC 141146667 in previous work⁴ by searching the TESS two-minute data³¹ for stars showing highly structured, periodic light curves. We selected the star for spectroscopy because its brightness and rotation rate enabled an efficient search for variability in its line profiles. We observed the star for five hours on 17 February 2024 (UT) using the High Resolution Echelle Spectrometer (HIRES³²) on the 10 m Keck I telescope. TESS observed the star over a four week interval from 30 January 2024 to 26 February 2024 with a duty cycle of 77%. During the HIRES observations, scattered light from the Earth caused a gap in the TESS photometry; TESS data collection resumed 12 hours (three rotation cycles) after the spectra were acquired. Extended Data Figure 1 shows the detailed photometric behavior of the star near the epoch of observation; the general photometric morphology is similar before and after the data gap.

2 Results

Figure 2 compiles the TESS and HIRES data from February 2024. Over timescales of years, CPVs maintain fixed periods while their photometric morphology evolves. TIC 141146667 indeed evolved relative to the February 2022 discovery data (see Figure 1). In February 2024, the average photometric signal showed a small brightening over 45% of the period, followed by a complex flux dip spanning 55% of the period. This eclipse feature shows two to three local photometric minima, and one to two local maxima. Its W-shape is suggestive of eclipse geometries seen in forward models of warped plasma tori (see³³ and the associated movies).

The spectroscopy shows emission beyond the star’s equatorial velocity ($v_{\text{eq}}=130 \text{ km s}^{-1}$). There are at least two distinct emission components, separated by half a cycle in phase. The inner component at lower velocities has clearer sinusoidal behaviour in time and is double-peaked, with peak semi-amplitudes of $2.07 v_{\text{eq}}$ and $2.88 v_{\text{eq}}$ (see § 3). There is significant non-periodic variability in the emissivity of this double-peaked component: the flux excess begins with an amplitude 70% that of the continuum early in the observation sequence, and diminishes to 10% by its end. The higher-velocity component 180° opposite in phase is detected only from $\phi=0.2$ – 1.0 . From $\phi=0.2$ – 0.5 , this outer component appears connected to the star in velocity space. While its peak semi-amplitude of $3.88 v_{\text{eq}}$ is achieved at both $\phi=0.25$ and 0.75 , its amplitude similarly

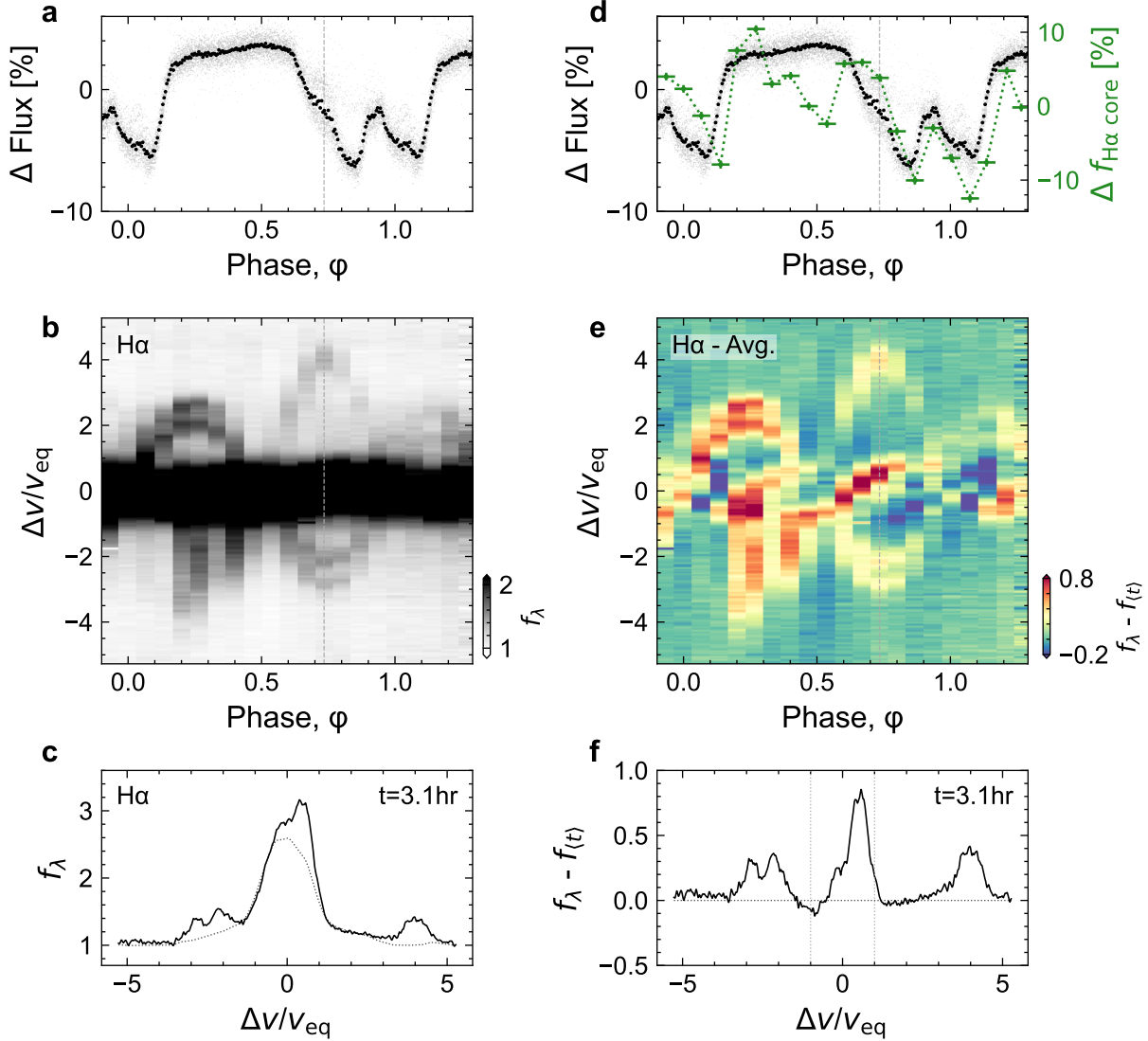


Figure 2 (Movie): Emission from circumstellar plasma orbiting TIC 141146667. The online movie, available [here](#), shows the spectral evolution over five hours. **a**, Average TESS light curve from 5 February 2024 to 26 February 2024 folded on the 3.930 hour period. Black points are phase-averaged; gray are the raw data. **b**, Keck/HIRES H α spectra acquired on 17 February 2024. The continuum is set to unity, and the darkest color is at twice the continuum to accentuate emission outside the line core ($|v/v_{\text{eq}}| > 1$, for $v_{\text{eq}}=130 \text{ km s}^{-1}$). While emission in the line core originates in the star’s chromosphere, the sinusoidal emission features are most readily described by a warped plasma torus. **c**, Individual epochs of Panel b, visible in the online movie. The dotted line shows the time-averaged spectrum, $f_{\langle t \rangle}$. **d**, As in Panel a, but overplotting the median-normalized H α light curve at $|v/v_{\text{eq}}| < 1$. **e**, As in Panel b, after subtracting the time-averaged spectrum. The line core shows H α excesses and decrements advancing from the blue to red wings. The asymmetric color stretch is set to mirror the dynamic range of the data. **f**, Individual epochs of Panel e, visible in the online movie.

decreases from a 60% excess over the continuum at the beginning of the observation sequence to a 10% excess by its end. The apparent period for all three spectroscopic emission components is consistent with the photometric 3.930 hour period.

These sinusoidal emission features require circumstellar clumps of partially-ionized hydrogen to corotate with the star. Based on the observed sinusoidal periods and velocities, this material's motion is not controlled by gravitational attraction to the star; it is more readily explained as a partially-ionized plasma being dragged along with a rigidly rotating stellar magnetic field. The velocity semi-amplitude of the sinusoids gives the mean distance of each clump from the stellar surface: $2.07 R_*$ and $2.88 R_*$ for the inner clumps, and $3.88 R_*$ for the outer clump. These clumps transit in front of the star when passing from negative to positive velocity. The transits of the two inner clumps last $\approx 22\%$ of each cycle, from $\phi = -0.1$ to $\phi = +0.12$ (see § 3). This spectroscopic transit coincides with the latter half of the complex eclipse feature in the TESS data.

The $H\alpha$ line core is more complex. At $|\Delta v/v_{\text{eq}}| < 1$, most observed $H\alpha$ photons come from the star's chromosphere; circumstellar material might also modulate the line profile. Figure 2e suggests line core variability caused by both bright and dark regions on the star's surface, superposed with smaller-amplitude variability from the transiting circumstellar material. For instance, from $\phi = 0-0.3$, the double-peaked emission feature is visible when viewed both on and off-limb; this feature is circumstellar in origin. However, the large emission feature that crosses the star from $\phi = 0.4-0.9$ emits at an amplitude greater than that observed from the circumstellar components, and it crosses the stellar velocity surface at a speed that suggests it instead originates from a chromospherically bright region on the star's surface. Similarly, from $\phi = 0.6-1.15$ a 20% deep absorption feature slowly crosses the $H\alpha$ line profile. This feature suggests either a chromospherically dark region (e.g. a starspot group) crossing the star's surface, or an azimuthally extended absorptive component to the circumstellar material which is not visible in emission. Although the origin of the other bright and dark streaks passing across the line core are similarly ambiguous, a final exercise to quantify the behavior of the line core is shown in Figure 2d, where $f_{H\alpha \text{ core}}$ denotes the summed flux at $|\Delta v/v_{\text{eq}}| < 1$. This panel shows that changes in the line core flux correlate with the broadband variability throughout most of the light curve, except near $\phi \approx 0.5$, corresponding to the transit of the $3.9 R_*$ clump and the occultation of the lower-velocity clump.

3 Discussion

Spectra of magnetically-active, rapidly rotating stars with a wide range of masses have been previously observed to exhibit both sinusoidal time-varying Balmer emission^{7,8,27,28} and transient absorption features^{6,25,36}, similar to Figure 2. No such stars were previously known to show complex light curves⁴. One interpretation for this spectroscopic variability comes from an analogy to quiescent solar prominences, which are cool condensations of plasma in the solar corona that can last days to weeks³⁷. These condensations fall back to the Sun's photosphere because gravity is stronger than any magnetic tension or centrifugal force capable of sustaining them. However for

Table 1: Selected system parameters for TIC 141146667

Parameter	Description	Value	Source
T_{eff}	Effective Temperature (K)	2972 ± 40	1
R_{\star}	Stellar radius (R_{\odot})	0.42 ± 0.02	1
Age	Stellar age range (Myr)	35-150	2
M_{\star}	Stellar mass (M_{\odot})	0.22 ± 0.02	3
γ	Systemic radial velocity (km s^{-1})	0.61 ± 1.47	4
SpT	Spectral Type	M5.5Ve	4
P_{rot}	Photometric rotation period (hr) .	3.930 ± 0.001	5
v_{eq}	Equatorial velocity ($2\pi R_{\star}/P_{\text{rot}}$) (km s^{-1})	130 ± 4	6
$v_{\text{eq}} \sin i_{\star}$	Projected rotational velocity (km s^{-1})	138 ± 8	4
v_{break} . . .	Breakup velocity ($GM_{\star}/R_{\star})^{1/2}$ (km s^{-1})	316 ± 16	6
i_{\star}	Stellar inclination 2σ lower limit (deg)	>63	4
d	Distance (pc)	57.54 ± 0.09	7
R_{c}	Keplerian corotation radius (R_{\star})	1.82 ± 0.10	6
a_0	Mean inner clump (0) orbital radius (R_{\star})	2.07 ± 0.04	4
a_1	Mean inner clump (1) orbital radius (R_{\star})	2.88 ± 0.10	4
a_2	Mean outer clump orbital radius (R_{\star})	3.88 ± 0.25	4
$\langle \text{EW}_{\text{H}\alpha} \rangle$	Time-averaged H α line core equivalent width (\AA)	7.2 ± 0.2	4

NOTE— Provenances are: 1: SED fit ⁴. 2: Gaia DR3 photometry shows the star is on the pre-main sequence, while the spectrum lacks lithium (see § 3). 3: PARSEC v1.2S ³⁴. 4: Keck/HIRES (see § 3). 5: TESS light curve. 6: Derived quantity. 7: Gaia DR3 geometric ³⁵.

stars with magnetospheric radii R_m that exceed their corotation radii R_c , the effective potential experienced by a charged particle can have a local minimum outside R_c , enabling the material to accumulate in a centrifugally-supported magnetosphere^{9,11}. Generally speaking, such material need neither transit nor be opaque in broadband optical light. In fact, Figure 2 suggests that the transits of the $H\alpha$ emitting material cannot explain the entirety of the complex photometric modulation; the spectroscopic transits happen too fast, and at orbital phases that only partially overlap with the photometric modulations.

Nonetheless, our Keck/HIRES observations are the first reported time-series spectra of a CPV, and they demonstrate that corotating circumstellar plasma clumps exist around at least one such star. While starspots likely do contribute smooth signals to the photometric variability, a “starspot-only” scenario for the CPVs⁵ is incompatible with our observations. Scenarios in which the circumstellar material is made only of dust are similarly ruled out. While starspots and dust may both be present, the observed $H\alpha$ emission requires clumps of plasma with a significant population of hydrogen atoms in the $n=3$ excited state, with most $H\alpha$ emission in each clump coming from a region half the size of the star (see § 3). The observed $H\alpha$ luminosity suggests characteristic densities and masses for the gaseous component of these clumps of $n_H \sim 10^{11} \text{ cm}^{-3}$ and $M_{\text{gas}} \sim 10^{17} \text{ g}$ (see § 3). Dust, if present, is independently constrained to have a total mass $10^{15} \text{ g} < M_{\text{dust}} < 10^{17} \text{ g}$ (see § 3). This circumstellar material could originate either from the star or from an external source. Plausible external sources include an undetected old disk, comets, or a close-in exoplanet. This latter scenario would make CPVs extrasolar analogs of the Jupiter-Io plasma torus (e.g. Ref. ³⁸).

The other potential analog for the CPVs are the σ Ori E variables, a rare subset of B stars with radiatively-driven winds which accumulate into warped plasma tori^{7,33}. These tori tend to have dense antipodal accumulations of plasma sculpted by tilted-dipole magnetic fields, and the transits of these clumps produce broadband photometric variability through bound-free scattering⁷ and Thomson scattering³⁹. The plasma accumulates at antipodes 180° apart because the deepest local minima in the effective potential exist along the line of intersection between the rotational and magnetic planes (see Equation 22 of ⁷). For σ Ori E and almost all of its analogs, the result is “simple” light curves that resemble those of eclipsing binaries, and time-dynamic $H\alpha$ spectra similar to those in Figure 2^{7,33}. The two known exceptions, HD 37776 and HD 64740, show complex light curves resembling CPVs^{4,40} and have spectropolarimetric magnetic field maps indicating strong contributions from higher-order magnetic moments^{41,42}. There are two implications: first, the photometric complexity of CPVs may be a direct consequence of magnetic fields with highly multipolar contributions. Second, despite this complexity, the observation (Figure 2) of two emission clumps separated 180° in phase is consistent with the expected emission from a warped plasma torus.

Pressing issues for future work include determining the composition and origin of the circumstellar material, understanding the exact role of the stellar magnetic field, and exploring the implied space weather experienced by the close-in rocky exoplanets that, statistically¹⁵, are likely

159 to be present in most CPV systems.

160 The material’s composition – either pure plasma or dusty plasma – can be clarified by time-
161 series optical and infrared spectrophotometry. While observations of CPVs in the optical suggest
162 a chromaticity consistent with dust ^{24,43,44}, a gray opacity source such as electron scattering in a
163 plasma transiting over a spotted background star might also produce chromatic features ⁴⁵. The
164 composition and size distribution of any dust that is present could be determined by measuring the
165 extinction curve for a sample of CPVs from 1-20 μm . Composition and size distributions similar
166 to debris from rocky bodies seen around white dwarfs ⁴⁶ would suggest an extrinsic origin channel.
167 Compositions and sizes similar to the interstellar medium would suggest that dust can condense
168 out from M dwarf winds, similar to processes that occur around more evolved stars ⁴⁷.

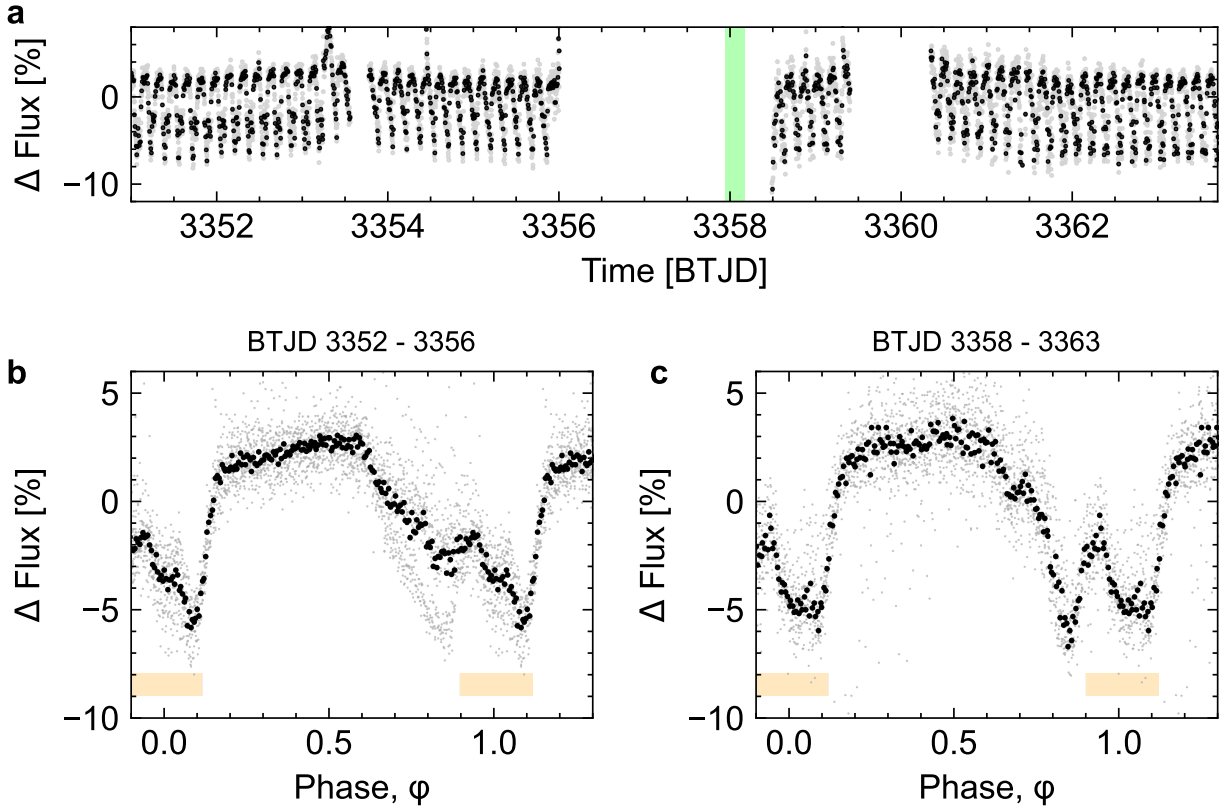
169 The role of the star’s magnetic field could be better understood through new observations,
170 and new theory. From the theoretical perspective, there is an urgent need for rigid-field magneto-
171 hydrodynamic modeling to go beyond previous work ^{7,33,48} and to explore what field topologies
172 might explain the observed light curve morphologies ⁴. In particular, dynamo simulations of fully-
173 convective M dwarfs have suggested that global-scale mean fields might be confined to a single
174 hemisphere ⁴⁹; such fields would yield accumulation surfaces quite different from those that have
175 previously been explored. Observationally, spectropolarimetry has the potential to assess both the
176 field strength and topology. An independent constraint on magnetic field topology may also come
177 from radio observations, which have shown ⁵⁰ that CPVs emit variable radio signals, including
178 persistent and polarized components. Detecting radio emission produced by an electron cyclotron
179 maser instability (e.g. ⁵¹) in particular would provide a measurement of the field strength at the site
180 of the emitting region, further clarifying the magnetosphere’s structure.

181 It is currently unclear what, if any, relationship CPVs have to the close-in rocky exoplanets
182 that exist around most M dwarfs ¹⁵. However, a few percent of young M dwarfs show the CPV
183 phenomenon ²⁰, and our data show that some of the complex photometric features occur when
184 clumps of circumstellar material transit the star. The suggested geometric correction implies that
185 an appreciable minority (10-30%) of young M dwarfs – the rapidly rotating ones with centrifu-
186 gal magnetospheres – host circumstellar environments similar to the CPVs. Future studies that
187 combine spectroscopic, polarimetric, and multi-wavelength observations, along with magnetohy-
188 drodynamic modeling, will be key to understanding the complex magnetospheric environments of
189 these young stars.

Methods

Observations & Data Reduction

Photometry: TESS observed TIC 141146667 ($T=13.3$) in Sectors 14, 15, 21, 41, 48, and 75. Two-minute data were acquired during Sectors 41, 48 (TESS DDT039, PI: Kunimoto), and 75 (TESS Program G06030, PI: Bouma). The data from Sectors 14, 15, and 21 had 30-minute cadence, which smears sharp features over the <4 hour period (see ²⁴). The field is not crowded: the nearest known star, TIC 141146666 ($T=14.5$), is $25''$ from TIC 141146667 and is photometrically stable in the pixel-level TESS data.



Extended Data Figure 1: Photometric evolution of TIC 141146667 near the Keck/HIRES observation (green bar). **a**, TESS simple aperture photometry. The main data gaps were caused by scattered light from the Earth (BTJD 3356-3358.5) and Moon (BTJD 3359.5-3360.5). Raw two minute data are in gray; black time-averages to ten minute sampling. **b-c**, Folded TESS light curve before and after spectroscopy. Raw two minute data are in gray; black phase-averages to 100 points per cycle. During BTJD 3352-3356, a state switch occurred near BTJD 3353, in which the dip at $\phi \approx 0.8$ disappeared. While the large eclipse feature was present both before and after the HIRES sequence, its photometric shape evolved during the data gap. The oranges bar denote times of spectroscopic transits for the inner two $H\alpha$ clumps observed with HIRES.

Extended Data Figure 1 shows the TESS Sector 75 data acquired near the epoch of spectroscopy. The gap in coverage from BTJD 3356.0 - 3358.5 occurred because the Earth was within 25° of the TESS camera’s boresight, yielding high levels of scattered light; this gap included the Keck/HIRES observation epoch (green bar). From BTJD 3359.4 - 3362.0, the Moon then passed within 25° of the camera’s boresight. Based on the observed level of scattered light in the optimal TIC 141146667 aperture, we manually masked out times from 3359.40 - 3360.13, and judged the remainder of the data during the lunar approach to be usable. Small data gaps from BTJD 3353.55 - 3353.77 and from BTJD 3360.12 - 3360.33 were caused by data downlinks at the spacecraft’s perigee and apogee, respectively.

Extended Data Figure 1 shows that a large, complex eclipse feature was present before and after the HIRES data were acquired. From BTJD 3352 - 3356, this eclipse had two sharp local minima; the local minimum at $\phi \approx 0.8$ disappeared following the flare at BTJD 3353, yielding an eclipse more closely resembling a long “V” than a “W”. Similar state changes have previously been noted and discussed^{2,4}. The photometric shape therefore evolved during the twelve cycles spanning the 3356 - 3358 gap, since the average shape from 3358-3363 more closely resembles the initial “W”.

Spectroscopy: We observed TIC 141146667 ($V=16.2$) with Keck/HIRES for five hours during the second half of the night, spanning 17 February 2024 10:47 to 16:13 (UT). The star’s airmass over this window spanned $z=1.2$ - 2.2 , and we opted for a fixed 15 minute cadence over the entire sequence, except for a final 10 minute exposure due to increasing sky brightness at sunrise. We observed without the iodine cell and used the C2 decker ($0''.86 \times 14''.0$) in the red instrument configuration, yielding a spectral resolution $R \approx 45,000$ ($\delta v \approx 6.7 \text{ km s}^{-1}$; $\delta v/v_{\text{eq}} \approx 0.05$). We binned the CCD readout by a factor of three in the spatial dimension, yielding $\approx 1,000$ photons (S/N=33) per pixel in the continuum at 6500 \AA , at minimum airmass. Strong winds contributed to $1''.2 \pm 0''.2$ seeing over the night, but conditions were otherwise favorable. We reduced the echelleogram to a one-dimensional spectrum using the standard techniques of the California Planet Survey⁵². Figure 2b shows the result in the vicinity of $H\alpha$ without any additional processing.

Stellar Parameters

Radial Velocity—We measured the radial velocities of TIC 141146667 from our HIRES spectra using a pipeline that we developed for rapidly rotating stars. Our method is based on template-matching against synthetic spectra produced by the PHOENIX stellar atmosphere code⁵³. We used the PHOENIX models with solar metallicity and alpha element abundances, and calibrated our pipeline using the standard stars described by⁵⁴. We used velocity standards spanning spectral types from G2 to M4 (Barnard’s Star), irrespective of rotation rate. We used *barycorrpy*⁵⁵ to calculate the velocity corrections due to Earth’s motion around the solar system barycenter and due to Earth’s daily rotation about its axis. Our analysis code reproduces the systemic velocities of known velocity standards⁵⁴ with an RMS of 0.66 km s^{-1} .

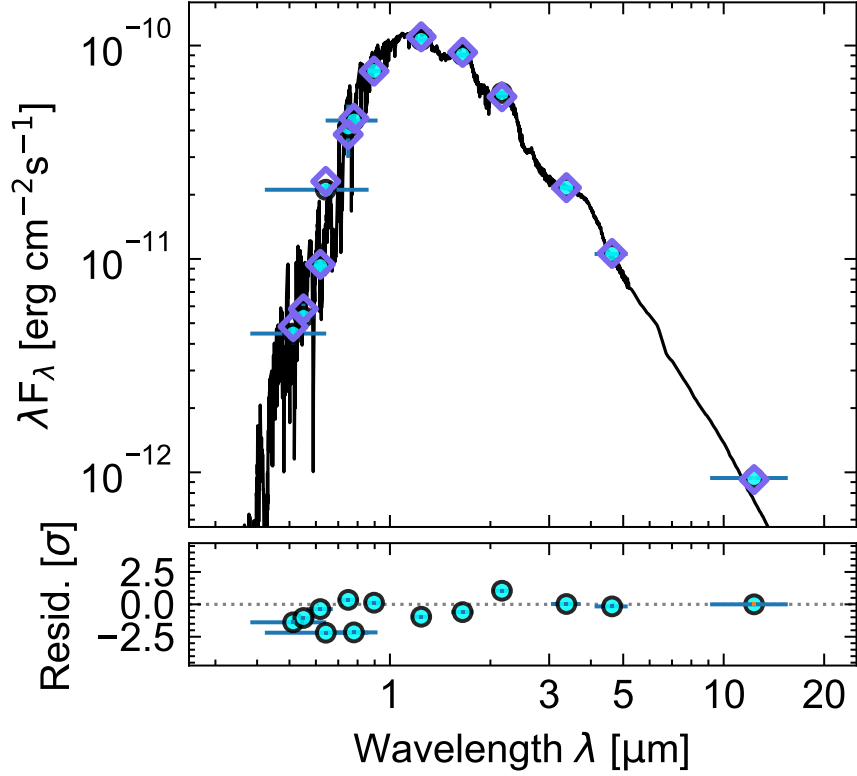
For TIC 141146667, we measured the radial velocities using regions near the K I (7700 \AA)

resonance line and three TiO bandheads (5160 Å, 5450 Å, and 5600 Å). We selected these regions because they provided the best matches between the synthetic and observed spectra. We then averaged the resulting redshift measurements over each order to produce the final measurement. We used the scatter of resulting velocity measurements between orders to assign the RV uncertainty at each epoch. The uncertainty-weighted mean systemic velocity over all epochs on 17 February 2024 was $\gamma = 0.6 \pm 1.5 \text{ km s}^{-1}$. The relative radial velocities about this mean are given in Table 2.

Viewing Orientation—We fitted the rotational broadening of the K I (7700 Å) resonance line using the kernel suggested by ⁵⁶; taking the mean and standard deviation of the resulting value over all epochs yielded $v_{\text{eq}} \sin i = 138 \pm 8 \text{ km s}^{-1}$, consistent with the visual line broadening $\Delta\lambda \approx 3 \text{ Å}$. The star’s equatorial velocity v_{eq} based on its apparent size and rotation period is $130 \pm 4 \text{ km s}^{-1}$. While this suggests that the viewing orientation could be nearly edge-on, the formal constraint is rather weak, with $i > 63^\circ$ at 2σ (2.5th percentile of the inclination posterior).

No Evidence For Binarity—Any periodicity in the radial velocity time-series is ruled out at the rotation period for semi-amplitudes above 2.85 km s^{-1} (at 3σ confidence). This sets an upper limit on the mass of any putative companion at the four hour period of $m \sin i < 2.4 M_{\text{Jup}}$. Regarding possible companions at wider separations, the Gaia DR3 renormalized unit weight error (RUWE), a proxy for the goodness of fit for a single-source astrometric model to the Gaia astrometry, is 1.23, within the usual range for apparently single sources. There are no resolved companions in the Gaia DR3 point source catalog. Finally, we checked the TESS light curve for evidence of secondary photometric periods by subtracting the mean CPV signal over each sector and performing a phase-dispersion minimization analysis ^{57,58}. There were no secondary periods in the TESS data. Previous work ⁴ has shown that about 30% of CPVs show evidence for excess noise above the Gaia single-source astrometric model, and about 40% of CPVs show evidence for unresolved binary companions based on the presence of secondary photometric periods. This agrees with analyses showing that multi-periodic low-mass stars are generally unresolved binaries ⁵⁹. Overall, the CPV binary fraction seems consistent with that for field M dwarfs ⁶⁰, pointing to a weak or non-existent connection between the CPV phenomenon and (wide) binarity. For TIC 141146667 specifically, although we find no evidence for stellar multiplicity, our data are minimally constraining for the scenario of a low-luminosity companion ($F_1/F_2 \lesssim 0.1$) with apparent separation below $0''.1$.

Effective temperature, radius, mass, and spectral classification—We adopted the star’s effective temperature and radius measured using the spectral energy distribution (SED) fitting procedure described by ⁴. To summarize, this approach used `astroARIADNE` ⁶² with the BT-Settl stellar atmosphere models ⁶¹, assuming the ⁶³ solar abundances and the ⁶⁴ water line lists. This approach fitted for the stellar effective temperature, radius, reddening, surface gravity, metallicity, and distance by comparing the measured broadband magnitudes against pre-computed model grids. Specifically, we performed the fit using the broadband magnitudes from Gaia DR2, APASS, 2MASS, SDSS, and WISE *W1* and *W2*. The resulting best-fit SED is shown in Extended Data Figure Figure 2. This method has the most constraining power for the star’s effective temperature ($2972 \pm 40 \text{ K}$) and radius ($0.42 \pm 0.02 R_\odot$); the surface gravity, metallicity, and reddening are



Extended Data Figure 2: Spectral energy distribution of broadband photometric magnitudes (filled markers) plotted over the best-fit BT-Settl stellar atmosphere model⁶¹ and the associated photometric predictions (empty markers). This plot was made from an adaptation of `astroARIADNE`⁶². The photometry extends from the Gaia DR3 blue passband to WISE W3; the W4 passband (22 μm) did not yield a confident detection. This fit yields the star’s temperature and size. The lack of excess infrared flux relative to the photospheric model sets an upper limit on emission from circumstellar dust.

only weakly constrained. We determined the star’s spectral type to be M5.5Ve by visually comparing the HIRES spectra against the photometric standards tabulated by⁶⁵. This result agrees with the effective temperature found from the SED fitting⁶⁶. We measured the equivalent width of the $\text{H}\alpha$ line by fitting a range of models to the time-averaged line profile shown in Figure 2, selecting the model that minimized the Bayesian information criterion, and numerically integrating this best fit model. We found a sum of two Gaussians to be the preferred model; our quoted result, $\text{EW}_{\text{H}\alpha} = 7.2 \pm 0.2 \text{ \AA}$, comes from numerically integrating within $|\Delta v/v_{\text{eq}}| < 1$. Integrating over the entire line profile, including the broad wings, would yield $\text{EW}_{\text{H}\alpha} = 10.2 \pm 0.3 \text{ \AA}$. Either value would classify the star as a weak-lined T Tauri⁶⁷.

Given the effective temperature, stellar radius, and age range (35-150 Myr) derived below, we then estimated the stellar mass by interpolating against the PARSEC v1.2S isochrones³⁴. Specifically, we used the distance metric defined in Equation 8 of⁴ to select the model mass closest to a

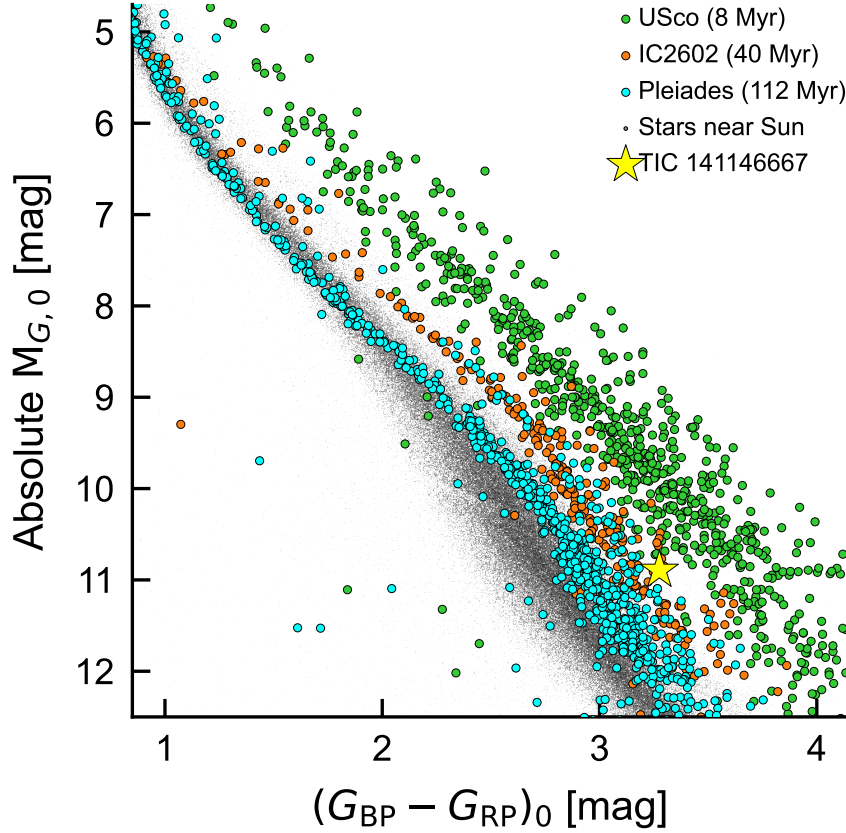
given observed temperature, radius, and age. This exercise yielded a mass of $M_\star = 0.20 \pm 0.01 M_\odot$ assuming an age of 35 Myr, or a mass of $0.25 \pm 0.01 M_\odot$ assuming an age of 150 Myr. These masses imply Keplerian corotation radii $R_{\text{cr}}/R_\star = 1.75 \pm 0.07$ and $R_{\text{cr}}/R_\star = 1.89 \pm 0.07$, respectively; this size scale is relevant because it is theoretically expected to set the inner boundary at which corotating material might accumulate (e.g. ^{7,11}). Our final quoted M_\star and R_{cr} values adopt the average of these extremes and a quadrature sum of their statistical uncertainties; we caution however that a more precise age would be needed to resolve the systematic uncertainties in these parameters.

Age: No Obvious Association Membership—Previous work ⁴ has found that over 90% of CPVs are associated with known young moving groups based on their positions and kinematics. TIC 141146667 is in the minority. We calculated the probability of TIC 141146667 being part of any nearby known group using BANYAN Σ v1.2 ⁶⁸. That particular model classifies it as a field star at >99.9% confidence. We also searched the local vicinity of TIC 141146667 for neighbors with similar projected on-sky velocities using `comove` ⁶⁹. This yielded no strong candidates for co-moving stars with projected tangential velocities $\Delta v_{\text{T}} < 5 \text{ km s}^{-1}$ that share its isochronal youth.

Age: Isochrones—The color and absolute magnitude of TIC 141146667 suggest that it is a pre-main sequence M dwarf, similar to all other known CPVs ^{2,4,70}. The star’s proximity ($d=58 \text{ pc}$) and high galactic latitude ($b=+53^\circ$) yield negligible interstellar reddening along the line of sight ⁷¹. Extended Data Figure 3 shows the location of TIC 141146667 in the color–absolute magnitude diagram (CAMD) relative to young stellar populations including Upper Scorpius (USco), IC 2602, and the Pleiades. To make this diagram, we adopted the USco members in the $\delta \text{ Sco}$ and $\sigma \text{ Sco}$ sub-associations from ⁷², and the IC 2602 and Pleiades members from ⁷³. We assumed an average V -band extinction $A_V = \{0.12, 0.11, 0.10\} \text{ mag}$ for USco ⁷⁴, IC 2602 ⁷³, and the Pleiades ⁷³ respectively, and ages of 8 Myr ⁷², 40 Myr ⁷⁵, and 112 Myr ⁷⁶ for each respective cluster. We dereddened the photometry using the extinction coefficients $k_X \equiv A_X/A_0$ tabulated in ⁷⁷, assuming that $A_0 = 3.1E(B - V)$.

Extended Data Figure 3 shows that TIC 141146667 falls between the USco and Pleiades sequences, and approximately overlaps IC 2602. However, the precision of the implied age is set by the intrinsic scatter of these calibration sequences; the most luminous stars in the Pleiades of the same color have a similar absolute magnitude as TIC 141146667. Previous work ⁷⁰ has also noted that in the Gaia passbands, CPVs tend to be photometrically redder and more luminous than single stars in any given cluster, similar to other rapid rotators. While this effect complicates any attempt at age inference based on the Gaia photometry, it suggests that the Pleiades may be a better comparison population than IC 2602. We take the star’s location in the color–absolute magnitude diagram to suggest age bounds $t_{\text{CAMD}} \sim 30\text{-}150 \text{ Myr}$.

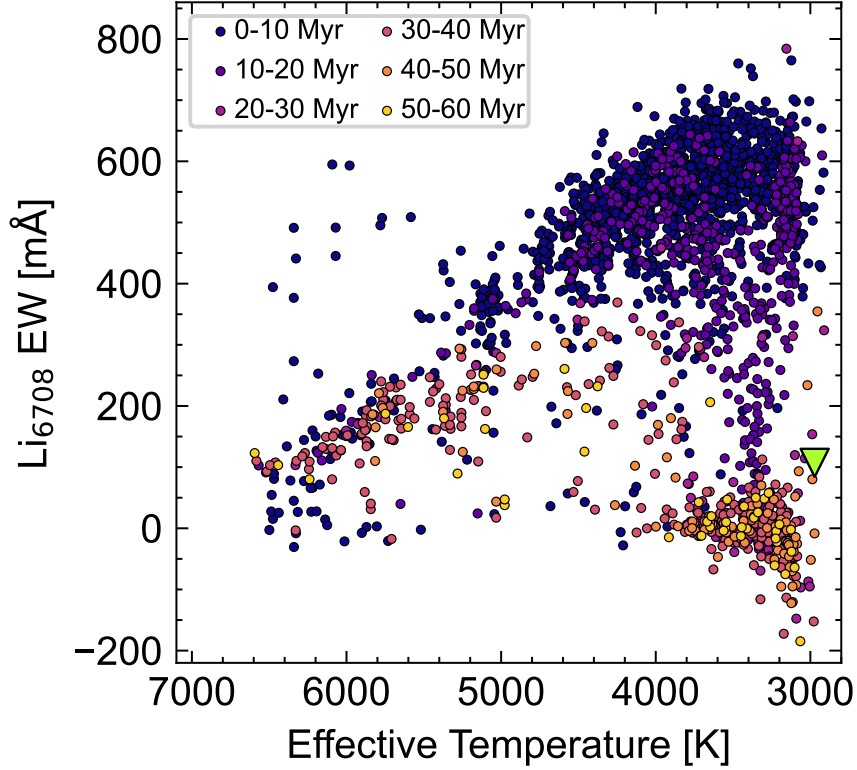
Age: Lithium—The depletion of lithium due to ${}^7\text{Li}(p, \alpha){}^4\text{He}$ burning in the cores of low-mass stars has been studied for over sixty years ^{78–80}. ⁸¹ provided a recent overview: an abbreviated summary is that sufficiently cool and young M dwarfs show the 6707.8 \AA doublet in absorption, $\gtrsim 10\%$ below their continua. However unlike for Sun-like stars, the continuum for M dwarfs is challenging to define due to their molecular absorption. We therefore attempted a lithium measurement



Extended Data Figure 3: Dereddened Gaia DR3 color vs. absolute magnitude diagram of TIC 141146667 and comparison samples. TIC 141146667 is on the pre-main sequence; stars with the same color on the main sequence are ≈ 1.5 magnitudes fainter. The star's location in this diagram suggests an age of 30-150 Myr.

by constructing a wavelength-binned and Doppler-corrected TIC 141146667 spectrum, assigning its uncertainties based on the measured scatter across the five hour dataset. We then compared this average spectrum against the nearest matching M6 template from ⁶⁵. The data show a small depression near the expected lithium wavelength, potentially consistent with the $\Delta\lambda \approx 3 \text{ \AA}$ line broadening. This feature nominally yields $\text{EW}_{\text{Li}} = 71^{+18}_{-13} \text{ m\AA}$, where the statistical uncertainties are evaluated using a bootstrap resampling technique from the statistical uncertainties in the HIRES spectrum. However, the systematic uncertainties associated with the continuum normalization are likely comparable to the amplitude of this feature; we therefore treat the result of this measurement as a 2σ upper limit: $\text{EW}_{\text{Li}} < 107 \text{ m\AA}$.

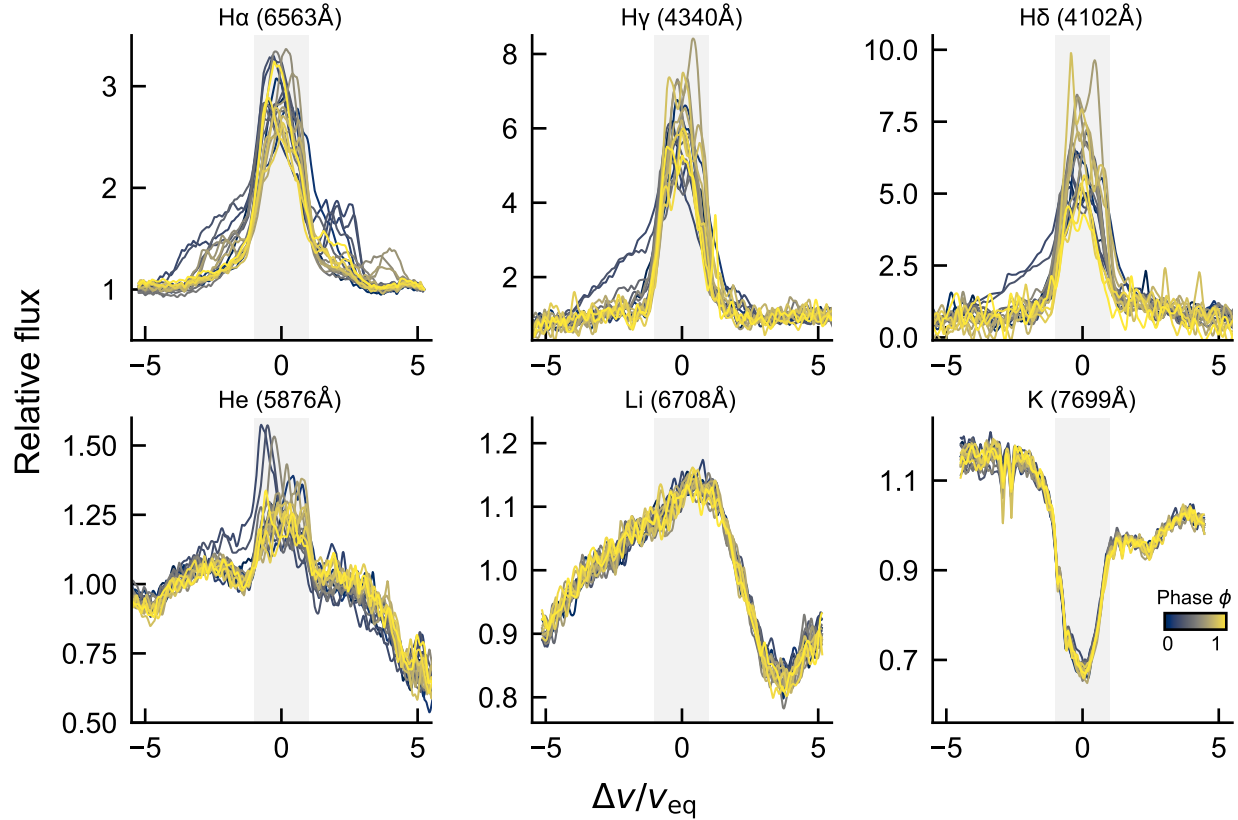
Despite uncertainties in the details, what can be stated with confidence is that lithium is not abundant in the spectrum of TIC 141146667. Extended Data Figure 4 compares our upper limit against the equivalent width measurements reported by ⁸² based on the Gaia-ESO spectroscopic survey; Extended Data Figure 5 shows the associated raw spectra. If the star were $\lesssim 20$ Myr old, at



Extended Data Figure 4: An upper limit on photospheric lithium for TIC 141146667 (green triangle) yields a lower bound on the star’s age of $\gtrsim 20$ Myr. Comparison stars are from the Gaia-ESO survey ⁸²; rich clusters in each age bin include NGC 2264 (4.5 Myr), λ Ori (8.7 Myr), γ^2 Vel (16.4 Myr), NGC 2547 (35.0 Myr), IC 2602 and IC 2391 (42.0 Myr), and NGC 2451A (50.0 Myr).

its temperature we would expect to see lithium in abundance (>400 mÅ). Since we do not, we can set an empirical bound on the lithium-derived age of $t_{\text{Li,emp}} \gtrsim 20$ Myr. The ⁸³ lithium isochrones provide a point for theoretical comparison, and suggest that since $M_K \approx 6.67$ mag, $t_{\text{Li,th}} \gtrsim 35$ Myr is the theoretical age at which complete depletion occurs in a star with this luminosity (see e.g. Figure 7 from ⁸¹).

Age: Summary—The main indicators for the youth of TIC 141146667 are *i*) that it is a complex periodic variable, and *ii*) that it is 1.5 magnitudes brighter (four times more luminous) than main sequence stars of the same color, while showing no indicators for binarity. Being a CPV suggests that the star is young because a previous CPV search unbiased in age found 90% of its detections to be in $\lesssim 200$ Myr old clusters ⁴; the remaining 10% were not associated with any coeval population. Similarly, studies of rotation in $\lesssim 100$ Myr clusters serendipitously found ≈ 50 -100 examples of the class ^{1–3, 19, 20, 70, 84–86}, whereas analogous studies of Praesepe and the Hyades did not report any evidence for CPVs in a set of approximately one thousand ≈ 700 Myr stars ^{87–89}. Regarding the isochronal age constraint, the Pleiades (112 Myr, ⁷⁶) shows a few stars of equal luminosity and the same temperature, suggesting a photometric isochronal age upper



Extended Data Figure 5: Time evolution of select regions in the Keck/HIRES spectra from 17 February 2024. We made this plot by applying a windowed outlier rejection to remove cosmic rays and then smoothing each spectrum with a Gaussian filter. The horizontal axis shows the velocity relative to each line’s rest wavelength, normalized by the stellar equatorial velocity. $H\alpha$ is the only Balmer line to show periodic variability of the form seen in Figure 2. The He 5876 Å line shows a time-dynamic blueshift that differs from the Balmer lines. Li 6708 Å shows no obvious absorption.

limit $\lesssim 150$ Myr. The weak lithium absorption suggests an age of at least 20 Myr based on an empirical comparison using Gaia-ESO spectra, or at least 35 Myr based on the 83 isochrones. These considerations yield our adopted age range of 35-150 Myr.

Spectroscopic Variability

Extended Data Figure 5 shows a few regions of interest in the HIRES spectra, which cover 3650-7960 Å. Higher order Balmer lines including $H\gamma$ and $H\delta$ ($n = 5 \rightarrow 2$ and $n = 6 \rightarrow 2$) do show variability outside the line core. However, this variability is not clearly periodic in the same manner as the emission seen in $H\alpha$. This could be because there are insufficient hydrogen ions in the relevant excited states, or because the spectra have lower precision in these bluer regions. The Ca HK doublet is also detected in emission, while the continuum near it is not. Chromospheric

emission from the magnesium triplet is also detected, but these lines are too blended to be usable.

Extended Data Figure 5 provides a novel view on the blue excess that appeared at $\phi \approx 0.2$ in $H\alpha$, $H\gamma$, $H\delta$, and He 5876 Å. At the same epoch, $H\alpha$ additionally shows a red clump of emission, and $H\gamma$ and $H\delta$ are also broadened on the red wing. The rise of this emission in <15 minutes might suggest a more sudden flow, rather than a stable, periodic component. For instance, a stellar flare might be connected to such a sudden rise. However, this idea seems incompatible with the sinusoidal emission seen later from $\phi \approx 0.5-1.0$, and with the fact that flares typically excite iron lines in the blue HIRES orders, which are not observed. More time-series spectroscopy would be needed to clarify this type of variability, in particular whether it is periodic or stochastic.

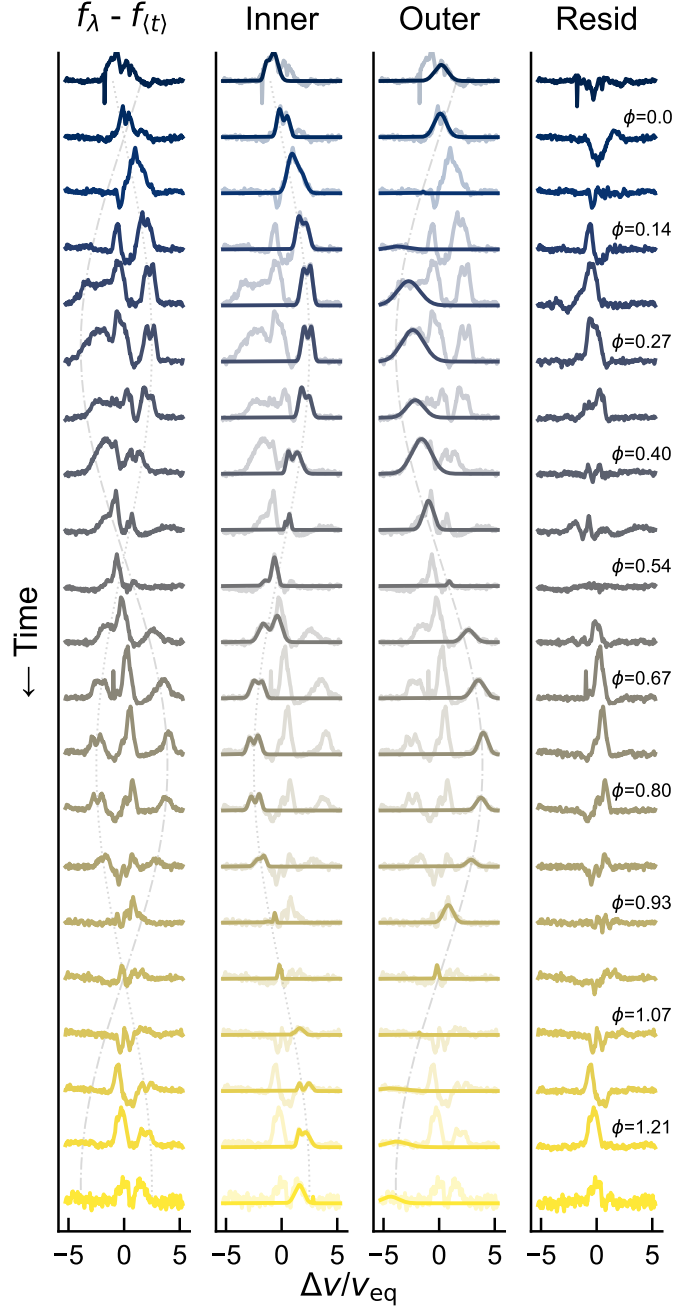
Finally, the Li I 6708 Å doublet, which shows no obvious absorption, as well as the broad K I 7699 Å resonance line are both visible in Extended Data Figure 5. In the latter, narrow telluric absorption features overlap the blue wing of the line. Neither of these regions shows any notable variability.

Detailed Behavior of $H\alpha$: Model and Implications

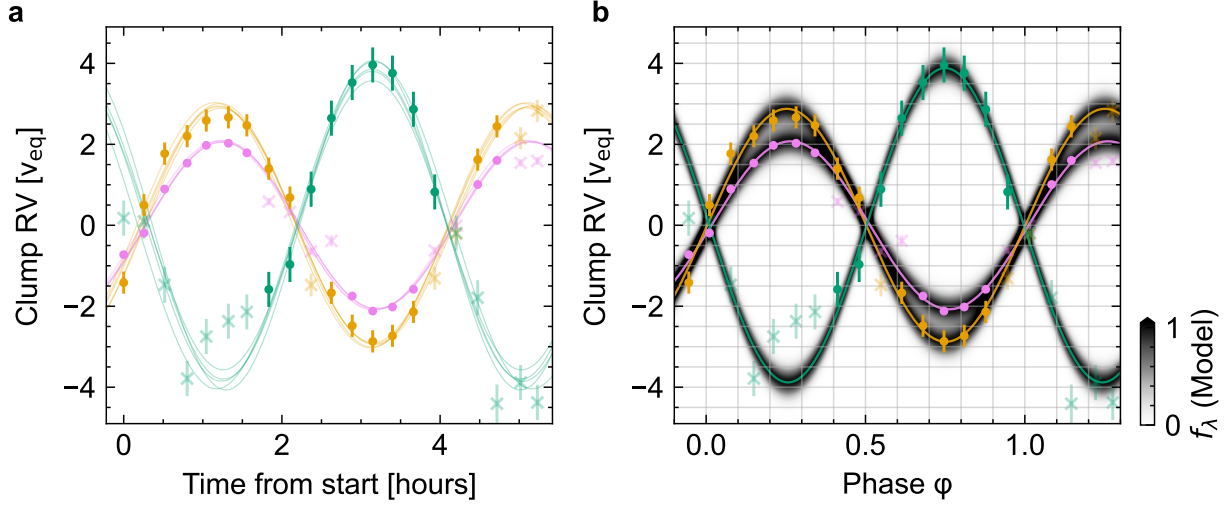
A model for the time-dynamic $H\alpha$ spectrum—While Figure 2 shows that clumps of circumstellar material exist around TIC 141146667, there is value in quantifying the exact orbital periods, velocities, and velocity dispersions of these clumps. These quantities can constrain the physical dimensions of the emitting region, and can also clarify whether the spectroscopic period agrees with the photometric period.

Given that a full radiative transfer simulation was outside our scope, we opted to construct a phenomenological model aimed at capturing the emission from the circumstellar material. We did this by fitting each spectral epoch with a multi-component gaussian, after having subtracted the time-average line profile as in Figure 2e. The results of this exercise are shown in Figure 6; details in the implementation and interpretation follow.

To implement the model, we assumed that the “inner” ($K_{\text{inner}} \approx 2.5 v_{\text{eq}}$) clump would be well-fit by a sum of two gaussians because it is visually double-peaked in the raw data from $\phi=0.15-0.35$ and $\phi=0.65-0.85$ (Figure 2b). We assumed that the “outer” ($K_{\text{outer}} \approx 3.9 v_{\text{eq}}$) clump would be better fit by a single gaussian, based on its behavior from $\phi=0.6-0.9$. Each gaussian component has three free parameters at each spectral epoch: the mean μ , standard deviation σ , and amplitude A . We labelled the inner component’s two gaussians $i = \{0, 1\}$, and the single outer component as $i = 2$. Given the complexity of the line profile data (Figure 6 left column), the likelihood function for this model is multimodal. We therefore imposed the prior constraints that $A_i \sim \mathcal{U}[0, 1]$, $\sigma_i/v_{\text{eq}} \sim \mathcal{U}[0, 1]$, and further assumed $\mu_i(t) \sim \mathcal{U}[K_{\text{inner}} \sin(\phi(t)) - v_{\text{eq}}, K_{\text{inner}} \sin(\phi(t)) + v_{\text{eq}}]$ for the inner two components, and $\mu_2(t) \sim \mathcal{U}[K_{\text{outer}} \sin(\phi(t) + \pi) - 2v_{\text{eq}}, K_{\text{outer}} \sin(\phi(t) + \pi) + 2v_{\text{eq}}]$ for the outer component. This prior on the means mitigates multimodality in the likelihood by requiring the mean velocity of each component to be within a one or two v_{eq} of the time-variable sinusoid suggested by visual inspection. We fitted each component to the data *independently* using



Extended Data Figure 6: Time-variable fit to H α line profiles. *Left column:* Raw spectrum at each epoch f_λ minus the time-averaged spectrum $f_{\langle t \rangle}$ (as in Figure 2e). Underplotted sinusoids are not fits; they are meant to guide the eye. *Middle columns:* Model of emission from the inner clump (sum of two gaussians) and the outer clump (single gaussian), plotted over the data. *Right column:* Residual of the left column after subtracting the sum of the two middle columns, leaving variability in the line core. § 3 discusses the use of this model.



Extended Data Figure 7: **a**, Orbits fit to mean radial velocities (RVs) extracted from H α profile fits in Figure 6. Radial velocities on the vertical axis are in units of the equatorial velocity, $v_{\text{eq}}=130 \text{ km s}^{-1}$. Each marker denotes the best-fit gaussian mean at a given epoch. Solid circles were adopted in the fits; transparent X markers were excluded due to reliability concerns (see text). The inner double-peaked clump is shown in violet and orange; the outer clump is shown in green. Five model draws from each posterior probability distribution are plotted. **b**, Idealized emissivity from mean model fits in Panel a, assuming a constant emission amplitude and velocity width $\sigma=0.25 v_{\text{eq}}$ over the observation sequence.

scipy’s non-linear least squares `curve_fit` implementation⁹⁰, and scaled the resulting parameter covariance matrix by a constant factor to match the sample variance of the residuals. The resulting means, amplitudes, and standard deviations for each component are given in Extended Data Table 3.

Caution is required in interpreting this model’s results. At certain epochs the most significant spectral feature around any component’s prior is not statistically significant. During such epochs, e.g. the “outer” clump at $\phi=1.07$, the model fits noise, not signal. At other times, the model underfits. For instance, the sudden blue rise near $\phi=0.2$ is poorly described by a gaussian; the assumed functional form is one of convenience. Finally, the model fits the $i = \{0, 1\}$, and $i = 2$ components independently. At $\phi=0.0$ and 1.0 , Figure 6 suggests that the emission might come from either the inner or outer components. Physically however, at this epoch the inner clump is in transit, and the outer clump is passing behind the star. At $\phi=0.0$, the double-peaked emission profile also matches that seen shortly afterward (at $\phi=0.14$) when the inner clump is viewed off-disk. A physical interpretation of the model would therefore discard the outer clump results at this particular epoch, because its emission would be blocked by the star.

Accounting for these caveats, we used the results from Extended Data Table 3 to quantify the orbital periods and velocity semi-amplitudes of the clumps. Figure 7a shows the results assuming

circular orbits; considering the Bayesian information criterion, we found no reason to prefer eccentric orbits. By visually inspecting Extended Data Figure 6, we excluded epochs where our gaussian profile fitting failed to either detect or else adequately represent the circumstellar emission. We then used NumPyro to sample the Gaussian likelihood for a Keplerian orbit with the NUTS algorithm⁹¹. We used the measurement uncertainties from each estimated mean radial velocity value and included an additional jitter term in quadrature. This procedure yielded orbital periods and semi-amplitudes of $P_0=3.92 \pm 0.03$ hr, $K_0/v_{\text{eq}}=2.07 \pm 0.04$; $P_1=3.92 \pm 0.06$ hr, $K_1/v_{\text{eq}}=2.88 \pm 0.10$; and $P_2=3.88 \pm 0.20$ hr, $K_1/v_{\text{eq}}=3.88 \pm 0.25$. The periods for the inner double-peaked clump are therefore consistent with the photometric 3.930 ± 0.001 hr period within a precision of two minutes. The “period” for the outer clump is ambiguous because the $\text{H}\alpha$ data only support the idea of a periodic orbit of material well-fit by gaussian emission from $\phi \approx 0.5$ -1.0. From $\phi=0$ -0.2, there is no detectable emission, and from $\phi=0.2$ -0.4, the emission spans 1 - $4 v_{\text{eq}}$ without taking a clear gaussian shape. While the outer-most edge of this $\phi=0.2$ -0.4 emission provides a plausible match to the expectation of a circular orbit, the idea of invoking a particular functional form for this component seems fine-tuned. We instead emphasize that although this emission is present, its variability in time is inconsistent with the idea of a stable clump of material. Additional observations would be needed to conclusively determine whether or not this component of the system is long-lived.

For Figure 7b, we then used the mean orbits from Figure 7a to generate sinusoidal-in-time gaussians, similar to the observations. We assumed a constant emission amplitude and velocity width $\sigma=0.25 v_{\text{eq}}$ for this exercise, and normalized each gaussian to unit amplitude; the colorbar in Figure 7b thus masks the non-physical additive contribution near the zero-crossing of velocity. Compared to the behavior of the data at $\phi=0.2$ -0.5 (Figure 2), this is highly idealized. Nonetheless, this exercise indicates that the transit of the inner clump lasts $\approx 22\%$ of each cycle, with a slight asymmetry around $\phi=0$.

Physical dimensions of the emitting region—The measured velocity widths from the circumstellar emission contain information about the size of the emitting region via the condition for rigid corotation. Consider a clump in cylindrical coordinates with arbitrary radial extent r , azimuthal extent ℓ , and height z . A range of shapes, including an “arc” with $\ell \gg r$, a “spoke” with $r \gg \ell$, and a “blob” with $r \approx \ell \approx z$ are all a priori possible. However, at quadrature, the observed velocity width of emission is sensitive to the radial extent of the circumstellar material. At mid-transit, the observed velocity width is sensitive to the azimuthal extent. An arc configuration would minimize the observed velocity width σ at quadrature, and maximize it during transit, with $\gtrsim 100 \text{ km s}^{-1}$ variations in between. This is not observed. The arc geometry, and by a similar argument the spoke geometry, can thus be discarded.

At quadrature, the inner clumps show $\sigma_i \approx 0.24 v_{\text{eq}}$, implying that 68% of the emission comes from a volume with length in the radial dimension $r_i = 2\sigma_i/\Omega = 0.48 R_\star$, and that 95% of the emission comes from within $0.96 R_\star$. These values have relative uncertainties of $\approx 5\%$, based on the uncertainties in the measured velocity dispersions. The two inner clumps are centered at orbital distances of $2.07 R_\star$ and $2.88 R_\star$. There is therefore physical overlap in their spatial distributions. These two clumps could in fact be a single clump with an optically thick $\text{H}\alpha$ line core. Regardless

of this nuance, the implication is that the full length in the radial dimension of these two inner emitting clumps is approximately equal to the star’s diameter. At mid-transit, these inner clumps likely have a similar velocity dispersion, although with greater uncertainty due to the differences between the $\phi=0$ and $\phi=1$ transits (see Extended Data Figure 6). This suggests a 1σ emission contour in the azimuthal dimension with a length of $\ell \approx 0.5 R_*$.

The vertical height of the emitting region is less constrained because the system is consistent with being viewed edge-on. However, one constraint does come if one assumes that the TESS transit depth scales with the projected $H\alpha$ emission area ℓz . More specifically, one can evaluate an “effective area” blocked by a two-dimensional gaussian blob passing over a star by integrating the local gaussian weight over the stellar surface. For instance, if $\ell \approx z \approx 0.24 R_*$, then $\iint \exp(- (x^2/2\sigma_x^2 + y^2/2\sigma_y^2)) dx dy$ suggests 11.5% of the star being “blocked”, a geometric factor which would need to be in turn multiplied by an unknown opacity factor to produce the observed transit depth ($\delta \approx 5\%$). In general though, there is a degeneracy between z and this opacity factor; larger vertical heights are allowed for lower optical depths in absorption, and vice-versa. This constraint also implicitly assumes that the optically thick material is well-mixed with the hydrogen, which may not be accurate.

Properties of the Plasma and Magnetospheric Environment

The physical conditions inside the plasma clumps, in particular the hydrogen number density, plasma temperature, ionization fraction, and magnetic field strength can be estimated from the available data. We caution that the following estimates are order of magnitude calculations that assume a simple uniform-density plasma: detailed considerations of radiative transfer are a worthy topic for future work, but are beyond the scope of this article.

Circumstellar $H\alpha$ emission might be sourced either from resonant scattering of stellar $H\alpha$ photons, or from radiative recombination. We neglect scattering because Figure 2 and Extended Data Figure 5 show the amplitude of the circumstellar $H\alpha$ emission varying by a factor of ≈ 5 , in a manner uncorrelated with any variability in the chromospheric line core. The volume emissivity under case B recombination can be written

$$j_{H\alpha} = n_e n_p \alpha_{H\alpha}^{\text{eff}} h\nu_{H\alpha}, \quad (1)$$

where n_e and n_p are the electron and proton densities, and $\alpha_{H\alpha}^{\text{eff}}$ is the effective recombination coefficient, defined to include all recombination routes that produce an $H\alpha$ photon. For hydrogen with temperatures between 1,000-10,000 K, $\alpha_{H\alpha}^{\text{eff}}$ is typically on the order of 10^{-12} to $10^{-13} \text{ cm}^3 \text{ s}^{-1}$ ^{92,93}. Neglecting the effects of atoms other than hydrogen, we can assume an ionization fraction x , such that $n_e = n_p = x n_H$, for n_H the hydrogen number density. Let $L_{H\alpha} = j_{H\alpha} V$, for V the volume of the emitting hydrogen. The luminosity of circumstellar hydrogen emission, $L_{H\alpha}$, is an observable: our SED fitting routine yields $L_* \approx 0.012 L_\odot$, which implies that the stellar $H\alpha$ line radiates at $\approx 1.0 \times 10^{28} \text{ erg s}^{-1}$. The luminosity of the clumps $L_{H\alpha}$ are of order one tenth that of the

star. If we approximate the emitting volume as a homogeneous sphere of radius r , we can write

$$n_{\text{H}} = 1 \cdot 10^{11} \text{ cm}^{-3} \left(\frac{0.5}{x} \right) \left(\frac{L_{\text{H}\alpha}}{10^{27} \text{ erg s}^{-1}} \frac{10^{-13} \text{ cm}^3 \text{ s}^{-1}}{\alpha_{\text{H}\alpha}^{\text{eff}}} \right)^{1/2} \left(\frac{0.1 R_{\odot}}{r} \right)^{3/2}. \quad (2)$$

For a uniform density clump, this suggests a total gas mass of $M_{\text{gas}} \approx 2 \times 10^{17} \text{ g}$. We emphasize that Equation 2 is intended to provide only an order of magnitude estimate for the number density implied by the observed H α emission. In detail, the effective recombination rate and the ionization fraction each vary with density and temperature; a more thorough estimate would iteratively solve the equations of detailed balance and radiative transfer (e.g. ⁶ Figure 8), and potentially also consider departures from local thermodynamic equilibrium.

Finally, a constraint on the magnetic field strength at the site of the clump follows from the requirement that the magnetic pressure exceed the thermal pressure, $B_c^2/8\pi > n_{\text{H}}kT$. Although we do not know the plasma temperature, if it were significantly beyond 1,000-10,000 K, we would either fully ionize the hydrogen, or not ionize enough of it. The field strength at the clump must therefore exceed

$$B_c \gtrsim 1 \text{ G} \left(\frac{n_{\text{H}}}{1 \times 10^{11} \text{ cm}^{-3}} \frac{T}{3000 \text{ K}} \right)^{1/2}. \quad (3)$$

Given that the average surface magnetic field strengths of low-mass stars have been measured to span hundreds to thousands of Gauss ⁹⁴⁻⁹⁶, this bound is easily met at orbital distances of 2-4 R_{\star} .

Upper and Lower Bounds on Dust

The material's composition – either pure plasma, or a dusty plasma – is not known. The idea of dust being present seems plausible given observations of chromatic transits in analogous objects ^{24,43,44}. However, this scenario is highly constrained. An upper limit on the amount of hot dust follows from the lack of an infrared excess. A lower limit follows if one assumes that most of the broadband optical depth comes from dust absorption and scattering, rather than any radiative processes associated with the plasma.

Regarding the upper limit, Extended Data Figure 2 shows the SED. While AllWISE ⁹⁷ yielded a confident W3 detection (9.8σ) consistent with the photospheric extrapolation from bluer bandpasses, the W4 extraction yielded only a marginal indication (1.7σ) of detectable flux. Similar to other CPVs ^{2,4}, the photometric uncertainties from WISE W1 and W2 allow at most a $\lesssim 2\%$ excess at 3-5 μm relative to the stellar photosphere, and a $\lesssim 5\%$ excess at 10 μm (W3). To estimate the implied mass bound, we assume a dust temperature $T_{\text{d}}=1500 \text{ K}$, typical for dust near the star (see ¹⁹ for discussion regarding dust sublimation). We then treat emission from the dust and star as Planck functions, and require $L_{\text{d}} < fL_{\star}$, where the factor f is set by the photometric precision of WISE and L_{d} is the bolometric dust luminosity. Given the reported uncertainties, we numerically find $f < 6 \cdot 10^{-3}$. From the Stefan-Boltzmann law we can then write $A_{\text{d}} < f(T_{\star}/T_{\text{d}})^4 Q_{\text{em}}^{-1} (4\pi R_{\star})^2$, for A_{d} the total emitting surface area of the dust, and Q_{em} an emission efficiency parameter. Converting this constraint to a dust mass requires an assumption regarding the grain properties. We assume a grain density $\rho_{\text{d}}=3 \text{ g cm}^{-3}$ typical for silicate grains, a fixed grain size $a=1 \mu\text{m}$, and no

self-absorption. This enables the assumption that $A_d = N\pi a^2$, for N the total number of dust grains. This in turn yields an upper limit on the dust mass of

$$M_{\text{dust}} \lesssim 4 \cdot 10^{17} \text{ g} \left(\frac{f}{6 \cdot 10^{-3}} \right) \left(\frac{T_\star}{3000 \text{ K}} \frac{1500 \text{ K}}{T_d} \right)^4 \left(\frac{Q_{\text{em}}}{1} \right)^{-1} \left(\frac{R_\star}{0.4 R_\odot} \right)^2 \left(\frac{a}{1 \mu\text{m}} \right) \left(\frac{\rho_d}{3 \text{ g cm}^{-3}} \right). \quad (4)$$

The analogous lower limit follows from requiring the optical depth from absorption and scattering τ to be at least unity. The optical depth can be written $\tau = n\sigma\ell$, where σ is the cross-section, n is the number density, ℓ is the path length. For spherical dust grains in the optical, $\sigma = Q_{\text{ext}}\pi a^2$, where Q_{ext} is the extinction efficiency parameter, tabulated e.g. by ⁹⁸ in their Figure 13. ⁹⁹ calculated the relevant cloud mass for this problem assuming a spherical dust clump of size r , and they found

$$M_{\text{dust}} \gtrsim 2 \cdot 10^{15} \text{ g} \left(\frac{\tau}{1} \right) \left(\frac{Q_{\text{ext}}}{3} \right)^{-1} \left(\frac{r}{0.1 R_\star} \frac{R_\star}{0.4 R_\odot} \right)^2 \left(\frac{a}{1 \mu\text{m}} \right) \left(\frac{\rho_d}{3 \text{ g cm}^{-3}} \right). \quad (5)$$

Three relevant objects for comparison include solar prominences, planetesimals, and comets. Prominences of the Sun have gas masses of 10^{14} g - 10^{16} g ³⁷. A planetesimal of mass $\approx 10^{15} \text{ g}$ with a bulk density of 1 g cm^{-3} would have a diameter of order one kilometer. Halley's comet has a mass of order 10^{17} g ¹⁰⁰, of which $\sim 10^{14} \text{ g}$ is shed per orbit, most of which inspirals toward the Sun due to Poynting-Robertson drag.

To summarize, if dust is responsible for the broadband variability of CPVs, it would need to be concentrated in clumps with masses in the range of 10^{15} - 10^{17} g . Given $M_{\text{gas}} \approx 2 \times 10^{17} \text{ g}$ from § 3, the allowed dust masses imply $M_{\text{gas}}/M_{\text{dust}}$ ranges of 1-100. More careful measurements of this ratio—in particular by inferring the dust mass through high precision infrared spectrophotometry—could provide a path for distinguishing the scenario of a trapped stellar outflow from an accumulation of externally-sourced material. While there are several plausible external sources, feeding through a low-mass disk in particular cannot be ruled out based on typical disk depletion times ¹⁰¹. Observations of infrared excesses and accretion signatures in low-mass stars tens of millions of years old suggest a broad lifetime distribution for such disks ^{102–105}.

1. Rebull, L. M. *et al.* Rotation in the Pleiades with K2. II. Multiperiod Stars. *Astron. J.* **152**, 114 (2016).
2. Stauffer, J. *et al.* Orbiting Clouds of Material at the Keplerian Co-rotation Radius of Rapidly Rotating Low-mass WTTs in Upper Sco. *Astron. J.* **153**, 152 (2017).
3. Rebull, L. M. *et al.* Rotation of Low-mass Stars in Upper Scorpius and ρ Ophiuchus with K2. *Astron. J.* **155**, 196 (2018).
4. Bouma, L. G. *et al.* Transient Corotating Clumps around Adolescent Low-mass Stars from Four Years of TESS. *Astron. J.* **167**, 38 (2024).

Parameter	Host	Source
Identifiers		
TIC	141146667	TESS
Gaia	860453786736413568	Gaia DR3
Astrometry & Radial Velocity		
α_{2000}	11:05:15.09	Gaia DR3
δ_{2000}	+59 15 05.57	Gaia DR3
μ_{α} (mas yr ⁻¹)	-73.933 \pm 0.022	Gaia DR3
μ_{δ} (mas yr ⁻¹)	32.262 \pm 0.024	Gaia DR3
π (mas)	17.324 \pm 0.025	Gaia DR3
RUWE	1.23	Gaia DR3
RV (km s ⁻¹)	0.61 \pm 1.47	HIRES
Photometry		
<i>TESS</i> (mag)	13.283 \pm 0.010	TIC8
<i>G</i> (mag)	14.701 \pm 0.002	Gaia DR3
<i>G</i> _{BP} (mag)	16.664 \pm 0.008	Gaia DR3
<i>G</i> _{RP} (mag)	13.398 \pm 0.006	Gaia DR3
<i>G</i> _{BP} - <i>G</i> _{RP} (mag)	3.276 \pm 0.010	Gaia DR3
<i>J</i> (mag)	11.401 \pm 0.022	2MASS
<i>H</i> (mag)	10.793 \pm 0.021	2MASS
<i>K</i> _s (mag)	10.473 \pm 0.016	2MASS
<i>W</i> 1 (mag)	10.276 \pm 0.023	ALLWISE
<i>W</i> 2 (mag)	10.070 \pm 0.020	ALLWISE
<i>W</i> 3 (mag)	9.838 \pm 0.045	ALLWISE
Physical Properties		
<i>T</i> _{eff} (K)	2972 \pm 40	SED fit ⁴
<i>R</i> _★ (<i>R</i> _☉)	0.42 \pm 0.02	SED fit ⁴
<i>L</i> _★ (<i>L</i> _☉)	0.0126 \pm 0.0012	SED fit ⁴
<i>P</i> _{rot} (hours)	3.930 \pm 0.001	TESS
<i>v</i> _{eq} (km s ⁻¹)	130 \pm 4	Derived
<i>v</i> _{eq} sin <i>i</i> _★ (km s ⁻¹)	138 \pm 8	HIRES
<i>i</i> _★ (°)	>63	Derived
<i>A</i> _V (mag)	0	⁷¹
<i>M</i> _★ (<i>M</i> _☉)	0.22 \pm 0.02	PARSEC ³⁴
EW _{Li} (mÅ)	<107	HIRES (2σ)
<i>t</i> _{CAMD} (Myr)	30-150	Gaia DR3
<i>t</i> _{Li,emp} (Myr)	>20	HIRES, ⁸²
<i>t</i> _{Li,th} (Myr)	>35	HIRES, ⁸³
<i>t</i> _{adopted} (Myr)	35-150	—

Extended Data Table 1: Properties of TIC 141146667. References: Gaia DR3 ³⁵, TESS ³¹, TIC8 ¹⁰⁶, 2MASS ¹⁰⁷, ALLWISE ⁹⁷.

Time [BJD _{TDB}]	RV (km s ⁻¹)	σ_{RV} (km s ⁻¹)
2460357.954919	2.73	5.86
2460357.965845	-4.40	2.37
2460357.976770	-0.19	2.64
2460357.987698	3.84	2.87
2460357.998619	7.53	7.53
2460358.009538	-1.98	1.44
2460358.020462	1.02	1.21
2460358.031383	0.64	7.03
2460358.042306	-2.91	2.71
2460358.053228	8.93	6.75
2460358.064154	5.95	8.84
2460358.075075	-2.25	3.06
2460358.085996	1.84	1.34
2460358.096918	2.41	8.24
2460358.107839	-7.04	3.94
2460358.118760	-2.24	3.07
2460358.129683	-2.83	7.55
2460358.140606	-0.59	2.26
2460358.151527	1.84	2.91
2460358.162448	4.54	3.95
2460358.173368	6.21	12.14

Extended Data Table 2: TIC 141146667 radial velocities relative to the systemic velocity based on the 7699 Å resonance line and TiO bandheads.

BTJD	μ_0	μ_1	μ_2	σ_0	σ_1	σ_2	A_0	A_1	A_2
3357.960099	-0.725 \pm 0.028	-1.416 \pm 0.026	0.177 \pm 0.019	0.39 \pm 0.03	0.18 \pm 0.03	0.59 \pm 0.02	0.51 \pm 0.01	0.23 \pm 0.04	0.29 \pm 0.01
3357.970746	-0.192 \pm 0.007	0.498 \pm 0.010	0.100 \pm 0.014	0.23 \pm 0.01	0.24 \pm 0.01	0.55 \pm 0.01	0.50 \pm 0.01	0.37 \pm 0.01	0.42 \pm 0.01
3357.981672	0.895 \pm 0.051	1.771 \pm 0.076	-1.470 \pm 0.113	0.40 \pm 0.02	0.40 \pm 0.10	0.09 \pm 0.11	0.67 \pm 0.05	0.34 \pm 0.04	0.03 \pm 0.03
3357.993524	1.536 \pm 0.011	2.202 \pm 0.015	-3.787 \pm 0.049	0.25 \pm 0.01	0.29 \pm 0.01	0.72 \pm 0.05	0.55 \pm 0.01	0.46 \pm 0.01	0.05 \pm 0.00
3358.003594	1.974 \pm 0.007	2.588 \pm 0.006	-2.749 \pm 0.020	0.26 \pm 0.01	0.22 \pm 0.00	1.00 \pm 0.02	0.64 \pm 0.01	0.67 \pm 0.01	0.43 \pm 0.01
3358.015249	2.027 \pm 0.003	2.666 \pm 0.003	-2.370 \pm 0.015	0.24 \pm 0.00	0.20 \pm 0.00	1.00 \pm 0.01	0.62 \pm 0.00	0.60 \pm 0.00	0.56 \pm 0.00
3358.024971	1.790 \pm 0.004	2.469 \pm 0.006	-2.138 \pm 0.011	0.24 \pm 0.00	0.26 \pm 0.00	0.77 \pm 0.01	0.53 \pm 0.00	0.38 \pm 0.00	0.31 \pm 0.00
3358.036522	0.584 \pm 0.008	1.399 \pm 0.009	-1.584 \pm 0.009	0.18 \pm 0.01	0.40 \pm 0.01	0.89 \pm 0.01	0.35 \pm 0.01	0.39 \pm 0.00	0.62 \pm 0.00
3358.047668	0.328 \pm 0.014	0.685 \pm 0.010	-0.969 \pm 0.017	0.07 \pm 0.01	0.13 \pm 0.01	0.46 \pm 0.02	0.14 \pm 0.02	0.28 \pm 0.02	0.52 \pm 0.02
3358.058824	-0.646 \pm 0.005	-1.474 \pm 0.066	0.891 \pm 0.079	0.23 \pm 0.00	0.25 \pm 0.07	0.14 \pm 0.08	0.51 \pm 0.01	0.10 \pm 0.01	0.09 \pm 0.04
3358.069519	-0.388 \pm 0.104	-1.669 \pm 0.023	2.646 \pm 0.020	0.40 \pm 0.07	0.40 \pm 0.02	0.53 \pm 0.02	0.47 \pm 0.04	0.33 \pm 0.01	0.22 \pm 0.01
3358.080468	-1.748 \pm 0.009	-2.483 \pm 0.010	3.526 \pm 0.009	0.25 \pm 0.01	0.33 \pm 0.01	0.55 \pm 0.01	0.28 \pm 0.01	0.32 \pm 0.00	0.32 \pm 0.00
3358.091255	-2.119 \pm 0.007	-2.868 \pm 0.007	3.960 \pm 0.005	0.26 \pm 0.01	0.23 \pm 0.01	0.40 \pm 0.01	0.34 \pm 0.01	0.29 \pm 0.01	0.39 \pm 0.00
3358.101671	-2.019 \pm 0.006	-2.731 \pm 0.008	3.758 \pm 0.005	0.20 \pm 0.01	0.24 \pm 0.01	0.43 \pm 0.01	0.29 \pm 0.01	0.25 \pm 0.01	0.23 \pm 0.00
3358.112713	-1.581 \pm 0.020	-2.141 \pm 0.043	2.867 \pm 0.019	0.19 \pm 0.02	0.29 \pm 0.03	0.40 \pm 0.02	0.18 \pm 0.02	0.13 \pm 0.01	0.12 \pm 0.00
3358.123928	-0.624 \pm 0.006	-1.312 \pm 0.076	0.824 \pm 0.012	0.09 \pm 0.01	0.22 \pm 0.08	0.44 \pm 0.01	0.18 \pm 0.01	0.02 \pm 0.01	0.32 \pm 0.01
3358.135236	-0.012 \pm 0.011	-0.208 \pm 0.012	-0.192 \pm 0.012	0.03 \pm 0.01	0.11 \pm 0.01	0.12 \pm 0.01	0.12 \pm 0.04	0.25 \pm 0.02	0.25 \pm 0.02
3358.146555	1.007 \pm 0.100	1.622 \pm 0.048	-1.789 \pm 0.045	0.06 \pm 0.11	0.31 \pm 0.06	0.04 \pm 0.05	0.02 \pm 0.04	0.12 \pm 0.02	0.05 \pm 0.05
3358.156693	1.603 \pm 0.018	2.444 \pm 0.024	-4.408 \pm 0.197	0.14 \pm 0.02	0.23 \pm 0.03	1.00 \pm 0.17	0.14 \pm 0.02	0.14 \pm 0.01	0.05 \pm 0.00
3358.169147	1.543 \pm 0.007	2.152 \pm 0.013	-3.885 \pm 0.031	0.14 \pm 0.01	0.39 \pm 0.01	1.00 \pm 0.04	0.23 \pm 0.01	0.27 \pm 0.00	0.10 \pm 0.00
3358.177978	1.588 \pm 0.037	2.828 \pm 0.005	-4.378 \pm 0.053	0.40 \pm 0.03	0.02 \pm 0.01	0.75 \pm 0.06	0.33 \pm 0.01	0.11 \pm 0.03	0.12 \pm 0.01

Extended Data Table 3: Best-fit parameters from multi-gaussian model fit to H α line profiles. These results should be treated with caution; only a subset of the spectral epochs yielded statistically significant detections of the circumstellar emission (see Extended Data Figure 6).

- 550 5. Koen, C. Starspot modelling of the TESS light curve of CVSO 30. *Astron. Astrophys.* **647**,
551 L1 (2021).
- 552 6. Collier Cameron, A. & Robinson, R. D. Fast H-alpha variations on a rapidly rotating cool
553 main sequence star- I. Circumstellar clouds. *Mon. Not. R. Astron. Soc.* **236**, 57–87 (1989).
- 554 7. Townsend, R. H. D. & Owocki, S. P. A rigidly rotating magnetosphere model for circumstel-
555 lar emission from magnetic OB stars. *Mon. Not. R. Astron. Soc.* **357**, 251–264 (2005).
- 556 8. Dunstone, N. J., Collier Cameron, A., Barnes, J. R. & Jardine, M. The coronal structure of
557 Speedy Mic - II. Prominence masses and off-disc emission. *Mon. Not. R. Astron. Soc.* **373**,
558 1308–1320 (2006).
- 559 9. Petit, V. *et al.* A magnetic confinement versus rotation classification of massive-star magne-
560 tospheres. *Mon. Not. R. Astron. Soc.* **429**, 398–422 (2013).
- 561 10. Waugh, R. F. P. & Jardine, M. M. Magnetic confinement of dense plasma inside (and outside)
562 stellar coronae. *Mon. Not. R. Astron. Soc.* **514**, 5465–5477 (2022).
- 563 11. Daley-Yates, S. & Jardine, M. M. Simulating stellar coronal rain and slingshot prominences.
564 *Mon. Not. R. Astron. Soc.* **534**, 621–633 (2024).
- 565 12. National Academies of Sciences, E. & Medicine. *Pathways to Discovery in Astron-*
566 *omy and Astrophysics for the 2020s* (The National Academies Press, Washington,
567 DC, 2023). URL [https://nap.nationalacademies.org/catalog/26141/](https://nap.nationalacademies.org/catalog/26141/pathways-to-discovery-in-astronomy-and-astrophysics-for-the-2020s)
568 [pathways-to-discovery-in-astronomy-and-astrophysics-for-the-2020s](https://nap.nationalacademies.org/catalog/26141/pathways-to-discovery-in-astronomy-and-astrophysics-for-the-2020s).
- 569 13. Redfield, S. *et al.* Report of the Working Group on Strategic Exoplanet Initiatives with HST
570 and JWST. *arXiv e-prints* arXiv:2404.02932 (2024).
- 571 14. TRAPPIST-1 JWST Community Initiative *et al.* A roadmap for the atmospheric characteri-
572 zation of terrestrial exoplanets with JWST. *Nature Astronomy* **8**, 810–818 (2024).
- 573 15. Dressing, C. D. & Charbonneau, D. The Occurrence of Potentially Habitable Planets Orbiting
574 M Dwarfs Estimated from the Full Kepler Dataset and an Empirical Measurement of the
575 Detection Sensitivity. *Astrophys. J.* **807**, 45 (2015).
- 576 16. Ribas, Á., Bouy, H. & Merín, B. Protoplanetary disk lifetimes vs. stellar mass and possible
577 implications for giant planet populations. *Astron. Astrophys.* **576**, A52 (2015).
- 578 17. France, K. *et al.* The MUSCLES Treasury Survey. I. Motivation and Overview. *Astrophys.*
579 *J.* **820**, 89 (2016).
- 580 18. Günther, M. N. *et al.* Stellar Flares from the First TESS Data Release: Exploring a New
581 Sample of M Dwarfs. *Astron. J.* **159**, 60 (2020).
- 582 19. Zhan, Z. *et al.* Complex Rotational Modulation of Rapidly Rotating M Stars Observed with
583 TESS. *Astrophys. J.* **876**, 127 (2019).

20. Rebull, L. M. *et al.* Rotation of Low-mass Stars in Taurus with K2. *Astron. J.* **159**, 273 (2020).
21. van Eyken, J. C. *et al.* The PTF Orion Project: A Possible Planet Transiting a T-Tauri Star. *Astrophys. J.* **755**, 42 (2012).
22. Johns-Krull, C. M. *et al.* H α Variability in PTFO8-8695 and the Possible Direct Detection of Emission from a 2 Million Year Old Evaporating Hot Jupiter. *Astrophys. J.* **830**, 15 (2016).
23. Bouma, L. G. *et al.* PTFO 8-8695: Two Stars, Two Signals, No Planet. *Astron. J.* **160**, 86 (2020).
24. Günther, M. N. *et al.* Complex Modulation of Rapidly Rotating Young M Dwarfs: Adding Pieces to the Puzzle. *Astron. J.* **163**, 144 (2022).
25. Collier Cameron, A. & Woods, J. A. Prominence activity in G dwarfs of the alpha Persei cluster. *Mon. Not. R. Astron. Soc.* **258**, 360–370 (1992).
26. Barnes, J. R., Collier Cameron, A., James, D. J. & Donati, J. F. Doppler images from dual-site observations of southern rapidly rotating stars - I. Differential rotation on PZ Tel. *Mon. Not. R. Astron. Soc.* **314**, 162–174 (2000).
27. Donati, J. F. *et al.* Surface differential rotation and prominences of the Lupus post T Tauri star RX J1508.6-4423. *Mon. Not. R. Astron. Soc.* **316**, 699–715 (2000).
28. Skelly, M. B. *et al.* Doppler images and chromospheric variability of TWA 6. *Mon. Not. R. Astron. Soc.* **385**, 708–718 (2008).
29. Leitzinger, M. *et al.* Indications of stellar prominence oscillations on fast rotating stars: the cases of HK Aqr and PZ Tel. *Mon. Not. R. Astron. Soc.* **463**, 965–979 (2016).
30. Cang, T. Q., Petit, P., Donati, J. F. & Folsom, C. P. Short-term variations of surface magnetism and prominences of the young Sun-like star V530 Per. *Astron. Astrophys.* **654**, A42 (2021).
31. Ricker, G. R. *et al.* Transiting Exoplanet Survey Satellite (TESS). *Journal of Astronomical Telescopes, Instruments, and Systems* **1**, 014003 (2015).
32. Vogt, S. S. *et al.* *SPIE Conference Series*, vol. 2198 (1994).
33. Townsend, R. H. D. Exploring the photometric signatures of magnetospheres around helium-strong stars. *Mon. Not. R. Astron. Soc.* **389**, 559–566 (2008).
34. Chen, Y. *et al.* Improving PARSEC models for very low mass stars. *Mon. Not. R. Astron. Soc.* **444**, 2525–2543 (2014).
35. Gaia Collaboration *et al.* Gaia Data Release 3. Summary of the content and survey properties. *Astron. Astrophys.* **674**, A1 (2023).

36. Cang, T. Q. *et al.* Magnetic field and prominences of the young, solar-like, ultra-rapid rotator V530 Persei. *Astron. Astrophys.* **643**, A39 (2020).
37. Vial, J.-C. & Engvold, O. *Solar Prominences*, vol. 415 of *Astrophysics and Space Science Library* (2015).
38. Bagenal, F. & Sullivan, J. D. Direct plasma measurements in the Io torus and inner magnetosphere of Jupiter. *J. Geophys. Res.* **86**, 8447–8466 (1981).
39. Berry, I. D., Owocki, S. P., Shultz, M. E. & ud-Doula, A. Electron scattering emission in the light curves of stars with centrifugal magnetospheres. *Mon. Not. R. Astron. Soc.* **511**, 4815–4825 (2022).
40. Mikulášek, Z. *et al.* What’s New with Landstreet’s Star HD 37776 (V901 Ori)? In Wade, G., Alecian, E., Bohlender, D. & Sigut, A. (eds.) *Stellar Magnetism: A Workshop in Honour of the Career and Contributions of John D. Landstreet*, vol. 11, 46–53 (2020). 1912.04121.
41. Kochukhov, O., Lundin, A., Romanyuk, I. & Kudryavtsev, D. The Extraordinary Complex Magnetic Field of the Helium-strong Star HD 37776. *Astrophys. J.* **726**, 24 (2011).
42. Shultz, M. E. *et al.* The magnetic early B-type stars I: magnetometry and rotation. *Mon. Not. R. Astron. Soc.* **475**, 5144–5178 (2018).
43. Tanimoto, Y. *et al.* Evidence for planetary hypothesis for PTFO 8-8695 b with five-year optical/infrared monitoring observations. *PASJ* **72**, 23 (2020).
44. Koen, C. Multifilter observations of the complex periodic variations in eight pre-main sequence stars. *Mon. Not. R. Astron. Soc.* **518**, 2921–2937 (2023).
45. Rackham, B. V., Apai, D. & Giampapa, M. S. The Transit Light Source Effect: False Spectral Features and Incorrect Densities for M-dwarf Transiting Planets. *Astrophys. J.* **853**, 122 (2018).
46. Reach, W. T., Lisse, C., von Hippel, T. & Mullally, F. The Dust Cloud around the White Dwarf G 29-38. II. Spectrum from 5 to 40 μm and Mid-Infrared Photometric Variability. *Astrophys. J.* **693**, 697–712 (2009).
47. Marigo, P. *et al.* Evolution of asymptotic giant branch stars. II. Optical to far-infrared isochrones with improved TP-AGB models. *Astron. Astrophys.* **482**, 883–905 (2008).
48. Krtićka, J., Mikulášek, Z., Kurfürst, P. & Oksala, M. E. Photometric signatures of corotating magnetospheres of hot stars governed by higher-order magnetic multipoles. *Astron. Astrophys.* **659**, A37 (2022).
49. Brown, B. P., Oishi, J. S., Vasil, G. M., Lecoanet, D. & Burns, K. J. Single-hemisphere Dynamos in M-dwarf Stars. *Astrophys. J.* **902**, L3 (2020).

50. Kaur, S. *et al.* Hints of auroral and magnetospheric polarized radio emission from the scallop-shell star 2MASS J05082729–2101444. *Astron. Astrophys.* **691**, L17 (2024).
51. Callingham, J. R. *et al.* The population of M dwarfs observed at low radio frequencies. *Nature Astronomy* **5**, 1233–1239 (2021).
52. Howard, A. W. *et al.* The California Planet Survey. I. Four New Giant Exoplanets. *Astrophys. J.* **721**, 1467–1481 (2010).
53. Husser, T. O. *et al.* A new extensive library of PHOENIX stellar atmospheres and synthetic spectra. *Astron. Astrophys.* **553**, A6 (2013).
54. Chubak, C. *et al.* Precise Radial Velocities of 2046 Nearby FGKM Stars and 131 Standards. *arXiv e-prints* arXiv:1207.6212 (2012).
55. Kanodia, S. & Wright, J. Python Leap Second Management and Implementation of Precise Barycentric Correction (barycorrpy). *Research Notes of the American Astronomical Society* **2**, 4 (2018).
56. Gray, D. F. *The Observation and Analysis of Stellar Photospheres* (2008).
57. Stellingwerf, R. F. Period determination using phase dispersion minimization. *Astrophys. J.* **224**, 953–960 (1978).
58. Bhatti, W. *et al.* waqasbhatti/astrobase: astrobase v0.5.3. Zenodo (2021).
59. Tokovinin, A. & Briceño, C. Yes, Multi-periodic Dwarfs in Upper Scorpius Are Binaries. *Astron. J.* **156**, 138 (2018).
60. Winters, J. G. *et al.* The Solar Neighborhood. XLV. The Stellar Multiplicity Rate of M Dwarfs Within 25 pc. *Astron. J.* **157**, 216 (2019).
61. Allard, F., Homeier, D. & Freytag, B. Models of very-low-mass stars, brown dwarfs and exoplanets. *Philosophical Transactions of the Royal Society A: Mathematical, Physical and Engineering Sciences* **370**, 2765–2777 (2012).
62. Vines, J. I. & Jenkins, J. S. ARIADNE: measuring accurate and precise stellar parameters through SED fitting. *Mon. Not. R. Astron. Soc.* **513**, 2719–2731 (2022).
63. Asplund, M., Grevesse, N., Sauval, A. J. & Scott, P. The Chemical Composition of the Sun. *ARA&A* **47**, 481–522 (2009).
64. Barber, R. J., Tennyson, J., Harris, G. J. & Tolchenov, R. N. A high-accuracy computed water line list. *Mon. Not. R. Astron. Soc.* **368**, 1087–1094 (2006).
65. Bochanski, J. J., West, A. A., Hawley, S. L. & Covey, K. R. Low-Mass Dwarf Template Spectra from the Sloan Digital Sky Survey. *Astron. J.* **133**, 531–544 (2007).

66. Pecaut, M. J. & Mamajek, E. E. Intrinsic Colors, Temperatures, and Bolometric Corrections of Pre-main-sequence Stars. *Astrophys. J. Suppl.* **208**, 9 (2013).
67. Briceuo, C. *et al.* The CIDA Variability Survey of Orion OB1. II. Demographics of the Young, Low-mass Stellar Populations. *Astron. J.* **157**, 85 (2019).
68. Gagné, J. *et al.* BANYAN. XI. The BANYAN Σ Multivariate Bayesian Algorithm to Identify Members of Young Associations with 150 pc. *Astrophys. J.* **856**, 23 (2018).
69. Tofflemire, B. M. *et al.* TESS Hunt for Young and Maturing Exoplanets (THYME). V. A Sub-Neptune Transiting a Young Star in a Newly Discovered 250 Myr Association. *Astron. J.* **161**, 171 (2021).
70. Stauffer, J. *et al.* Even More Rapidly Rotating Pre-main-sequence M Dwarfs with Highly Structured Light Curves: An Initial Survey in the Lower Centaurus-Crux and Upper Centaurus-Lupus Associations. *Astron. J.* **161**, 60 (2021).
71. Green, G. M., Schlafly, E., Zucker, C., Speagle, J. S. & Finkbeiner, D. A 3D Dust Map Based on Gaia, Pan-STARRS 1, and 2MASS. *Astrophys. J.* **887**, 93 (2019).
72. Ratzenbock, S. *et al.* Significance mode analysis (SigMA) for hierarchical structures. An application to the Sco-Cen OB association. *Astron. Astrophys.* **677**, A59 (2023).
73. Hunt, E. L. & Reffert, S. Improving the open cluster census. III. Using cluster masses, radii, and dynamics to create a cleaned open cluster catalogue. *Astron. Astrophys.* **686**, A42 (2024).
74. Pecaut, M. J. & Mamajek, E. E. The star formation history and accretion-disc fraction among the K-type members of the Scorpius-Centaurus OB association. *Mon. Not. R. Astron. Soc.* **461**, 794–815 (2016).
75. Randich, S. *et al.* The Gaia-ESO Survey: open clusters in Gaia-DR1 . A way forward to stellar age calibration. *Astron. Astrophys.* **612**, A99 (2018).
76. Dahm, S. E. Reexamining the Lithium Depletion Boundary in the Pleiades and the Inferred Age of the Cluster. *Astrophys. J.* **813**, 108 (2015). URL <https://ui.adsabs.harvard.edu/abs/2015ApJ...813..108D>.
77. Gaia Collaboration *et al.* Gaia Data Release 2. Summary of the contents and survey properties. *Astron. Astrophys.* **616**, A1 (2018).
78. Hayashi, C. & Nakano, T. Evolution of Stars of Small Masses in the Pre-Main-Sequence Stages. *Progress of Theoretical Physics* **30**, 460–474 (1963).
79. Bildsten, L., Brown, E. F., Matzner, C. D. & Ushomirsky, G. Lithium Depletion in Fully Convective Pre-Main-Sequence Stars. *Astrophys. J.* **482**, 442–447 (1997).

80. Burke, C. J., Pinsonneault, M. H. & Sills, A. Theoretical Examination of the Lithium Depletion Boundary. *Astrophys. J.* **604**, 272–283 (2004).
81. Wood, M. L. *et al.* TESS Hunt for Young and Maturing Exoplanets (THYME). IX. A 27 Myr Extended Population of Lower Centaurus Crux with a Transiting Two-planet System. *Astron. J.* **165**, 85 (2023).
82. Jeffries, R. D. *et al.* The Gaia-ESO Survey: empirical estimates of stellar ages from lithium equivalent widths (EAGLES). *Mon. Not. R. Astron. Soc.* **523**, 802–824 (2023).
83. Feiden, G. A. Magnetic inhibition of convection and the fundamental properties of low-mass stars. III. A consistent 10 Myr age for the Upper Scorpius OB association. *Astron. Astrophys.* **593**, A99 (2016).
84. Stauffer, J. *et al.* More Rapidly Rotating PMS M Dwarfs with Light Curves Suggestive of Orbiting Clouds of Material. *Astron. J.* **155**, 63 (2018).
85. Rebull, L. M. *et al.* Rotation of Low-mass Stars in Upper Centaurus-Lupus and Lower Centaurus-Crux with TESS. *Astron. J.* **164**, 80 (2022).
86. Popinchalk, M. *et al.* Examining the Rotation Period Distribution of the 40 Myr Tucana-Horologium Association with TESS. *Astrophys. J.* **945**, 114 (2023).
87. Rebull, L. M. *et al.* Rotation of Late-type Stars in Praesepe with K2. *Astrophys. J.* **839**, 92 (2017).
88. Douglas, S. T. *et al.* K2 Rotation Periods for Low-mass Hyads and a Quantitative Comparison of the Distribution of Slow Rotators in the Hyades and Praesepe. *Astrophys. J.* **879**, 100 (2019).
89. Rampalli, R. *et al.* Three K2 Campaigns Yield Rotation Periods for 1013 Stars in Praesepe. *Astrophys. J.* **921**, 167 (2021).
90. Virtanen, P. *et al.* SciPy 1.0: fundamental algorithms for scientific computing in Python. *Nature Methods* **17**, 261–272 (2020).
91. Phan, D., Pradhan, N. & Jankowiak, M. Composable Effects for Flexible and Accelerated Probabilistic Programming in NumPyro. *arXiv e-prints* arXiv:1912.11554 (2019).
92. Hummer, D. G. & Storey, P. J. Recombination-line intensities for hydrogenic ions - I. Case B calculations for H I and He II. *Mon. Not. R. Astron. Soc.* **224**, 801–820 (1987).
93. Draine, B. T. *Physics of the Interstellar and Intergalactic Medium* (2011).
94. Donati, J. F. & Landstreet, J. D. Magnetic Fields of Nondegenerate Stars. *ARA&A* **47**, 333–370 (2009).
95. Kochukhov, O. Magnetic fields of M dwarfs. *A&A Rev.* **29**, 1 (2021).

96. Reiners, A. *et al.* Magnetism, rotation, and nonthermal emission in cool stars. Average magnetic field measurements in 292 M dwarfs. *Astron. Astrophys.* **662**, A41 (2022).
97. Cutri, R. M. *et al.* VizieR Online Data Catalog: AllWISE Data Release (Cutri+ 2013). *VizieR Online Data Catalog* II/328 (2021).
98. Croll, B. *et al.* Multiwavelength Observations of the Candidate Disintegrating Sub-Mercury KIC 12557548b. *Astrophys. J.* **786**, 100 (2014).
99. Sanderson, H., Jardine, M., Collier Cameron, A., Morin, J. & Donati, J. F. Can scallop-shell stars trap dust in their magnetic fields? *Mon. Not. R. Astron. Soc.* **518**, 4734–4745 (2023).
100. Rickman, H. The nucleus of comet Halley: Surface structure, mean density, gas and dust production. *Advances in Space Research* **9**, 59–71 (1989).
101. Haisch, K. E., Jr., Lada, E. A. & Lada, C. J. Disk Frequencies and Lifetimes in Young Clusters. *Astrophys. J.* **553**, L153–L156 (2001).
102. Silverberg, S. M. *et al.* Peter Pan Disks: Long-lived Accretion Disks Around Young M Stars. *Astrophys. J.* **890**, 106 (2020).
103. Lee, J., Song, I. & Murphy, S. 2MASS J15460752-6258042: a mid-M dwarf hosting a prolonged accretion disc. *Mon. Not. R. Astron. Soc.* **494**, 62–68 (2020).
104. Gaidos, E. *et al.* Planetesimals around stars with TESS (PAST) - II. An M dwarf ‘dipper’ star with a long-lived disc in the TESS continuous viewing zone. *Mon. Not. R. Astron. Soc.* **514**, 1386–1402 (2022).
105. Pfalzner, S. & Dincer, F. Low-mass Stars: Their Protoplanetary Disk Lifetime Distribution. *Astrophys. J.* **963**, 122 (2024).
106. Stassun, K. G. *et al.* The Revised TESS Input Catalog and Candidate Target List. *Astron. J.* **158**, 138 (2019).
107. Skrutskie, M. F. *et al.* The Two Micron All Sky Survey (2MASS). *Astron. J.* **131**, 1163–1183 (2006).

Acknowledgments LGB is grateful to M. Jardine, A. Weinberger, B. Tofflemire, J. Spake, J. Winn, and L. Hillenbrand for insightful conversations that significantly informed this work, and to A. Howard and H. Isaacson for their assistance reducing the HIRES spectra. This work was supported by the Carnegie Fellowship and by the Heising-Simons 51 Pegasi b Fellowship. Funding for the TESS mission is provided by NASA’s Science Mission directorate. TESS is a product of millions of hours of work by thousands of people; we thank the TESS team for their efforts to make the mission a continued success. The HIRES data were obtained at the Keck Observatory, which exists through a similar scale of community effort. We recognize the importance that the summit of Maunakea has always had within the indigenous Hawaiian community, and we are deeply grateful for the opportunity to conduct observations from this mountain.

781 **Data Availability** The TESS two-minute cadence data used in this work are publicly available from
782 the Mikulski Archive for Space Telescopes (MAST; <https://mast.stsci.edu>). The Keck/HIRES
783 spectra analyzed here are accessible via the Keck Observatory Archive (KOA; [https://koa.ipac.](https://koa.ipac.caltech.edu)
784 [caltech.edu](https://koa.ipac.caltech.edu)).

785 **Competing Interests** The author declares no competing financial interests.

786 **Correspondence** Correspondence and requests for materials should be addressed to Luke Bouma, at either
787 lbouma@carnegiescience.edu or bouma.luke@gmail.com.